

Planck-LFI instrument description

M. Bersanelli^{1,2}, N. Mandolesi³, R.C. Butler³, A. Mennella^{1,2}, F. Villa³, B. Aja⁴, E. Artal⁴, E. Artina⁵, C. Baccigalupi⁶, M. Balasini⁵, G. Baldan⁵, A. Banday⁷, P. Bastia⁵, P. Battaglia⁵, T. Bernardino⁸, E. Blackhurst⁹, L. Boschini⁵, C. Burigana³, G. Cafagna⁵, B. Cappellini^{1,2}, F. Cavaliere¹, F. Colombo⁵, G. Crone¹⁰, F. Cuttaia³, O. D’Arcangelo¹¹, L. Danese⁶, R. Davies⁹, R. Davis⁹, L. De Angelis¹², G.C. De Gasperis¹³, L. De La Fuente⁴, A. De Rosa³, G. De Zotti¹⁴, M.C. Falvella¹², F. Ferrari⁵, R. Ferretti⁵, L. Figini¹¹, F. Fogliani¹⁵, C. Franceschet¹, E. Franceschi³, T. Gaier¹⁶, S. Garavaglia¹¹, F. Gomez¹⁷, K. Gorski¹⁶, A. Gregorio¹⁸, P. Guzzi⁵, J.M. Herreros¹⁷, R. Hoyland¹⁷, N. Hughes¹⁹, M. Janssen¹⁶, P. Jukkala¹⁹, D. Kettle⁹, V.H. Kilpiä¹⁹, M. Laaninen²⁰, P.M. Lapolla⁵, C.R. Lawrence¹⁶, D. Lawson⁹, P. Leahy⁹, R. Leonardi²¹, P. Leutenegger⁵, S. Levin¹⁶, P.B. Lilje²², S. Lowe⁹, P.M. Lubin²¹, D. Maino¹, M. Malaspina³, M. Maris¹⁵, J. Marti-Canales¹⁰, E. Martinez-Gonzalez⁸, A. Mediavilla⁴, P. Meinhold²¹, M. Miccolis⁵, G. Morgante³, P. Natoli¹³, R. Nesti²³, L. Pagan⁵, C. Paine¹⁶, B. Partridge²⁴, J.P. Pascual⁴, F. Pasian¹⁵, D. Pearson¹⁶, M. Pecora⁵, F. Perrotta¹⁵, P. Platania¹¹, M. Pospieszalski²⁵, T. Poutanen^{26,27,28}, M. Prina¹⁶, R. Rebolo¹⁷, N. Roddis⁹, J.A. Rubino¹⁷, M.J. Salmon⁸, M. Sandri³, M. Seiffert¹⁶, R. Silvestri⁵, A. Simonetto¹¹, P. Sjöman¹⁹, G.F. Smoot²⁹, C. Sozzi¹¹, L. Stringhetti³, J. Tauber⁸, L. Terenzi³, M. Tomasi¹, J. Tuovinen³⁰, L. Valenziano³, J. Varis²⁸, N. Vittorio¹³, L. Wade¹⁶, A. Wilkinson⁹, F. Winder⁹, A. Zacchei¹⁵, and A. Zonca^{1,2}

¹ Università degli Studi di Milano, Dipartimento di Fisica, Milano, Italy

² IASF - Sezione di Milano, INAF, Milano, Italy

³ IASF - Sezione di Bologna, INAF, Bologna, Italy

⁴ Departamento de Ingeniera de Comunicaciones, Universidad de Cantabria, Spain

⁵ Thales Alenia Space - Italia, Vimodrone, Milano, Italy

⁶ SISSA, Trieste, Italy

⁷ MPA, Max Planck Inst. für Astrophysik, Garching, Germany

⁸ Instituto de Fisica De Cantabria, Consejo Superior de Investigaciones Científicas, Universidad de Cantabria, Spain

⁹ Jodrell Bank Observatory, Jodrell Bank, U.K

¹⁰ ESA-E TEC, Noordwijk, Netherlands

¹¹ Istituto di Fisica del Plasma, CNR, Milano, Italy

¹² Agenzia Spaziale Italiana (ASI)

¹³ Università di Roma Tor Vergata, Italy

¹⁴ Osservatorio Astronomico di Padova, INAF, Italy

¹⁵ Osservatorio Astronomico di Trieste, INAF, Italy

¹⁶ Jet Propulsion Laboratory, Pasadena, USA

¹⁷ Instituto de Astrofísica de Canarias, Tenerife, Spain

¹⁸ Dipartimento di Fisica, Università degli Studi di Trieste, Italy

¹⁹ DA-Design Oy, Jokioinen, Finland

²⁰ Ylinen Electronics Oy, Kauniainen, Finland

²¹ University of California at Santa Barbara, Physics Department, USA

²² Institute of Theoretical Astrophysics, University of Oslo, Norway

²³ Osservatorio Astrofisico di Arcetri, Firenze, INAF, Italy

²⁴ Haverford College, USA

²⁵ National Radio Astronomy Observatory, Charlottesville, USA

²⁶ University of Helsinki, Department of Physics, Helsinki, Finland

²⁷ Helsinki Institute of Physics, Helsinki, Finland

²⁸ Metsähovi Radio Observatory, Helsinki University of Technology, Kylmäla, Finland

²⁹ Lawrence Berkeley National Laboratory, Berkeley, USA

³⁰ MilliLab, VTT Technical Research Centre of Finland, Espoo, Finland

ABSTRACT

Aims. In this paper we present the Low Frequency Instrument (LFI), designed and developed as part of the Planck space mission, the ESA program dedicated to precision imaging of the cosmic microwave background (CMB). Planck-LFI will observe the full sky in intensity and polarisation in three frequency bands centred at 30, 44 and 70 GHz, while higher frequencies (100-850 GHz) will be covered by the HFI instrument (Lamarre et al 2009).

Methods. The LFI is an array of microwave radiometers based on state-of-the-art Indium Phosphide cryogenic HEMT amplifiers implemented in a differential system using internal blackbody loads as reference signals. The front-end is cooled to 20K for optimal sensitivity and the reference loads are cooled to 4K to minimise low frequency noise.

Results. We provide an overview of the LFI instrument, discuss the leading scientific requirements and describe the design solutions adopted for the various hardware subsystems. The main drivers of the radiometric, optical and thermal design are discussed, including the stringent requirements on sensitivity, stability, and rejection of systematic effects. Greater details on the key instrument units and the results of ground calibration are provided in a set of companion papers.

Key words. Cosmology, Cosmic microwave background, Space instrumentation, Radiometers, Instrument design and calibration

1. Introduction

Observations of the cosmic microwave background (CMB) have played a central role in the enormous progress of cosmology in the past few decades. Technological developments in both coherent radio receivers and bolometric detectors supported an uninterrupted chain of successful experiments, from the initial discovery (Penzias & Wilson 1965) up to the present generation of precision measurements. Following COBE¹ and WMAP², the Planck³ mission is a third generation satellite entirely dedicated to CMB observations. The Planck instruments are designed to extract all the cosmological information encoded in the CMB temperature anisotropies with an accuracy set by cosmic variance and ultimate astrophysical confusion limits, and to push polarisation measurements well beyond previously reached results. Planck will image the sky in nine frequency bands across the CMB blackbody peak, leading to a full-sky map of the CMB temperature fluctuations with signal-to-noise >10 and angular resolution <10 arcmin. The Planck instruments and observing strategy are devised to reach an unprecedented combination of angular resolution ($5'$ to $30'$), sky coverage (100%), spectral coverage (27-900 GHz), sensitivity ($\Delta T/T \sim 10^{-6}$), calibration accuracy ($\sim 0.5\%$), rejection of systematic effects ($\sim 1\mu\text{K}$ per pixel) (Tauber et al 2009a). In addition, all Planck bands between 30 and 350 GHz will be sensitive to linear polarisation.

The imaging power of Planck is sized to extract the temperature power spectrum with high precision over the entire angular range dominated by primordial fluctuations. This will lead to accurate estimates of cosmological parameters that describe the geometry, dynamics and matter-energy content of the universe. The Planck polarisation measurements are expected to deliver complementary information on cosmological parameters and to provide a unique probe of the thermal history of the universe in the early phase of structure formation. Planck will also test the inflationary paradigm with unprecedented sensitivity through studies of non-Gaussianity and of B-mode polarisation as a signature of primordial gravitational waves⁴.

The Planck wide frequency range (30-850 GHz) is primarily required to ensure accurate discrimination of foreground emissions from the cosmological signal. However, the nine Planck maps will also represent a rich data set for galactic and extragalactic astrophysics. Up to now, no single technology can reach the required performances in the entire Planck frequency range. For this reason two complementary instruments are integrated at the Planck focal plane exploiting state-of-the-art radiometric and bolometric detectors in their best windows of operation. The Low Frequency Instrument (LFI), described in this paper, covers the 27-77 GHz range with a radiometer array cooled to 20K. The High Frequency Instrument (HFI) will observe in six bands in the 90-900 GHz range with a bolometer array cooled to 0.1K (Lamarre et al (2009)). The two instruments share the focal plane of a single telescope, a shielded

off-axis dual reflector Gregorian system with 1.5×1.9 m primary aperture (Tauber et al 2009a).

The design of the Planck satellite and mission plan is largely driven by the extreme thermal requirements imposed by the instruments. The cold payload enclosure (~ 50 K passive cooling) needs to be thermally decoupled from the warm (~ 300 K) service module while preserving high thermal stability. The optical design, orbit and scanning strategy are optimised to obtain the required effective angular resolution, rejection of straylight and environmental stability. Planck will be injected into a Lissajous orbit around the Sun-Earth L2 point, at 1.5 million km from Earth. The scanning strategy assumes, to first order, the spacecraft spinning at 1 rpm with the spin axis aligned at 0° solar aspect angle (see Tauber et al 2009a for details). The typical angle between the detectors line of sight and the spin axis is $\sim 85^\circ$. It will be possible to redirect the spin axis within a cone of 10° around the spacecraft-sun axis. The baseline mission allows for 14 months of routine scientific operations in L2, a period in which the entire sky can be imaged twice by all detectors. However, in anticipation of a possible extension of the mission, spacecraft and instrument consumables allow an extension by at least a factor of two.

In this paper we provide an overall description of the Planck-LFI, discuss its scientific requirements and design solutions. We present an overview of the main subsystems, particularly those that are critical for scientific performance, while referring to a set of companion papers for more details. The LFI program as a whole, including data processing and programmatic issues, is described in Mandolesi et al. (2009); the LFI calibration plan and ground calibration results are discussed by Mennella et al. (2009) and Villa et al. (2009a). The LFI optical design is presented in (Sandri et al. 2009), while the expected polarisation performances are discussed in (Leahy et al (2009)).

2. Scientific requirements

In this section we will discuss the main scientific requirements for the LFI. In the following sections we shall describe the design solutions implemented to meet such requirements.

2.1. Frequency range

The minimum of the combined emission of foregrounds relative to the CMB spectrum occurs at $\lambda \sim 4$ mm, i.e., roughly at the turning point between optimal performances of radiometric coherent receivers and bolometric detectors. Simulations carried out in the early design phases of Planck⁵ showed that a set of four logarithmically spaced bands in the 30-100 GHz would provide a good spectral leverage to disentangle low frequency components while covering the window of minimum foregrounds for optimal CMB science. The LFI is designed to cover the frequency range downstream the peak of the CMB spectrum using an array of differential radiometers. The initial Planck-LFI configuration (Mandolesi et al. 2000b) included four bands

Send offprint requests to: M. Bersanelli:
marco.bersanelli@mi.infn.it

¹ <http://lambda.gsfc.nasa.gov/product/cobe/>

² <http://map.gsfc.nasa.gov/>

³ <http://www.rssd.esa.int/Planck>

⁴ For a detailed description of the scientific objectives of planck see ESA-SCI(2005)1 ("Planck bluebook")

⁵ See ESA D/SCI (96), COBRAS/SAMBA Report on Phase A Study, 1996.

centered at 30, 44, 70 and 100 GHz, with the 100 GHz channel being covered by both LFI and HFI for scientific redundancy and systematics crosscheck. Budget and managerial difficulties, however, led to descopeing of the LFI 100 GHz channel, which is now covered by HFI only. Nonetheless, the three LFI bands centred at 30, 44 and 70 GHz in combination with the six HFI bands provide Planck with a uniquely broad spectral coverage for robust separation of non-cosmological components. In addition, the LFI 70 GHz channel offers the cleanest view of the CMB for both temperature and polarisation anisotropy.

2.2. Angular resolution and sensitivity

Neglecting astrophysical foregrounds, calibration errors and systematic effects, the uncertainty in the CMB power spectrum C_ℓ is given by:

$$\frac{\delta C_\ell}{C_\ell} = f_{\text{sky}}^{-1/2} \sqrt{\frac{2}{2\ell+1}} \left[1 + \frac{A\sigma_{\text{pix}}^2}{N_{\text{pix}}C_\ell W_\ell^2} \right], \quad (1)$$

where f_{sky} is the fraction of CMB sky observed, A is the surveyed area, N_{pix} is the number of pixels, σ_{pix} is the average noise per pixel at end of mission, and W_ℓ is the window function, which for LFI can be approximated by $W_\ell^2 = \exp[-\ell(\ell+1)\sigma_B^2]$ with $\sigma_B = \theta_{\text{FWHM}}/\sqrt{8\ln 2} = 1.235 \times 10^{-4} \theta_{\text{FWHM}}$ and θ_{FWHM} is the full width half maximum of the beam, assumed Gaussian. For a given mission lifetime, the sensitivity per pixel in thermodynamic temperature is given by:

$$\sigma_{\text{pix}} = \frac{\Delta T}{\sqrt{n_{\text{rad}} \tau_{\text{pix}}}}, \quad (2)$$

where ΔT is the sensitivity per unit bandwidth of an array with n_{rad} radiometers over an average integration time:

$$\tau_{\text{pix}} = \frac{\tau_{\text{mission}}}{N_{\text{pix}}} = \frac{\tau_{\text{mission}}}{4\pi/\theta_{\text{FWHM}}^2}. \quad (3)$$

2.2.1. Angular resolution

The basic scientific requirement for the Planck angular resolution is to provide approximately 10' beams in the lowest foreground window, and to achieve up to 5' in the highest frequency channels. This led to a telescope in the 1.5 m aperture class to ensure the desired resolution with an adequate rejection of straylight contamination (Mandolesi et al. 2000a; Villa et al. 2002). In general, a trade-off occurs between main beam resolution (half-power beam width, HPBW) and the illumination by the feeds of the edges of both the primary and sub-reflector (edge taper) which in turn drives the stray-light contamination effect. An edge taper >30 dB at an angle of 22° and an angular resolution of 14' at 70 GHz were set as design specifications for LFI. Detailed calculations taking into account the location of the feeds in the focal plane and the telescope optical performance (Sandri et al. 2009) showed that angular resolutions of $\sim 13'$ are achieved for the 70 GHz channels, while at lower frequencies we expect 24'–28' at 44 GHz (depending on channel) and $\sim 33'$ at 30 GHz.

Table 1. LFI specifications for sensitivity and angular resolution. ΔT_{30} indicates the noise per 30' reference pixel. Sensitivities per pixel are specified for nominal mission survey time of 15 months.

	30 GHz	44 GHz	70 GHz
ΔT_{30} (μK)	8	8	8
$\Delta T_{30}/T$	3×10^{-6}	3×10^{-6}	3×10^{-6}
Angular resolution (arcmin)	33	24	14
$\Delta T/T$ per pixel (frequency array)	2.6×10^{-6}	3.6×10^{-6}	6.2×10^{-6}
Number of feeds	2	3	6
Number of radiometers	4	6	12
$\delta T_{1\text{sec},A}$ ($\mu\text{K} \times \sqrt{\text{s}}$) ^a	234	278	365
$\delta T_{1\text{sec}}$ ($\mu\text{K} \times \sqrt{\text{s}}$) ^b	239	292	414
Effective bandwidth (GHz)	6	8.8	14
System noise temperature T_{sys} (K) ^b	10.7	16.6	29.2

^a Antenna temperature

^b Thermodynamic temperature

2.2.2. Sensitivity

To specify noise per frequency channel we adopted the general criterion of uniform sensitivity per equivalent pixel. In the early design phases, based on extrapolation of previous technological progress, we set a noise specification $\Delta T_{30}/T = 3 \times 10^{-6}$ (or $\Delta T_{30} = 8 \mu\text{K}$, thermodynamic temperature) for a reference pixel $\Delta\theta_{30} \equiv 30'$ at all frequencies. We have also considered “goal” sensitivities of $\Delta T_{30} = 6 \mu\text{K}$ per reference pixel, i.e., lower by 30%.

With an array of $n_{\text{rad},\nu}$ radiometers at frequency ν a sky pixel will be observed, on average, for an integration time

$$\tau_{\text{tot},\nu} = n_{\text{rad},\nu} \frac{\tau_{\text{mission}} \theta_{\text{pix},\nu}^2}{4\pi} \quad (4)$$

Assuming a 14 months survey, for $\Delta T_{30} = 8 \mu\text{K}$ the sensitivity per pixel for a 1-s integration time is given by $\delta T_{1\text{sec}} \simeq 120 \mu\text{K} \times \sqrt{n_{\text{rad},\nu}}$. We chose $n_{\text{rad},\nu}$ to compensate the higher noise temperatures at higher frequencies and allocated 4 radiometers at 30 GHz, 6 at 44 GHz and 12 at 70 GHz.

As we will describe in detail in Sect. 3, the LFI receivers are coupled in pairs to each feed horn ($n_{\text{rad}} = 2n_{\text{feeds}}$) through an orthomode transducer. Thus the LFI design is such that all channels are inherently sensitive to polarisation. The sensitivity to Q and U Stokes parameters is lower than the sensitivity to total intensity I by a factor $\sqrt{2}$ since the number of channels per polarisation is only half as great. In order to optimise the LFI sensitivity to polarisation, the location and orientation of the LFI radiometers in focal plane needs to follow well defined constraints, as it will be described in Sect. 4. In Table 1 we summarise the main requirements for LFI sensitivity and angular resolution and first order design choices.

2.3. Sensitivity budget

For an array of coherent receivers, each with typical bandwidth $\Delta\nu$ and noise temperature T_{sys} , the average white noise per pixel (in antenna temperature) will be:

$$\delta T_{\text{pix},A} = k_R \frac{T_{\text{sys}} + T_{A,\text{Sky}}}{\sqrt{\Delta\nu_{\text{eff}} \cdot \tau_{\text{tot}}}}, \quad (5)$$

where $k_R = \sqrt{2}$ for the LFI pseudo-correlation receivers. Therefore, for a required $\delta T_{\text{pix},A}$, the 1-second sensitivity (in antenna temperature) of each radiometer must be:

$$\delta T_{1\text{sec},A}(\mu\text{K}\sqrt{s}) < \delta T_{\text{pix},A} \sqrt{n_{\text{rad}} \frac{\tau_{\text{mission}}}{N_{\text{pix}}}}, \quad (6)$$

where $N_{\text{pix}} = 4\pi/\theta_{\text{pix}}^2$ is the number of pixels.

2.3.1. Bandwidth and system noise

A first breakdown for contributions to LFI sensitivity is between system temperature and effective bandwidth. Each radiometer is characterised by a spectral response $g(\nu)$ which is determined by the overall spectral response of the system including amplifiers, waveguide components, filters, etc. We define the radiometer effective bandwidth as:

$$\Delta\nu_{\text{eff}} = \frac{[\int_0^\infty g(\nu)d\nu]^2}{\int_0^\infty g^2(\nu)d\nu} \quad (7)$$

In general, ripples in the band tend to narrow the ideal rectangular equivalent bandwidth. We assume for LFI a goal effective bandwidth of 20% of the centre frequency. Equation 5 then leads to requirements on T_{sys} of ~ 10 K at 30 GHz, and ~ 30 K at 70 GHz (see Table 2).

2.3.2. Active cooling

These very ambitious noise temperatures can only be achieved with cryogenically cooled low noise amplifiers. Typically, the noise temperature of current state-of-the-art cryogenic transistor amplifiers exhibit a factor of 4-5 reduction going from 300 K to 100 K operating temperature, and another factor 2÷2.5 from 100 K to 20 K. We implement active cooling to 20 K of the LFI front-end (including feeds, OMTs and first-stage amplification) to gain in sensitivity and to optimise the LFI-HFI thermo-mechanical coupling in the focal plane.

Because the cooling power of the 20 K cooler (see Sect. 5) is not compatible with the full radiometers operating at cryogenic temperature, each radiometer has been split into a 20 K front-end module and a 300 K back-end module, each carrying about half of the needed amplification (~ 70 dB overall). A set of waveguides connect the front and back-end modules, which have been designed to provide sufficient thermal decoupling between the cold and warm sections of the instrument. Furthermore, low power dissipation components are required in the front-end. This is ensured by the new generation of cryogenic Indium Phosphide (InP) high electron mobility transistor (HEMT) devices, which yield world-record low noise performances with very low power dissipation.

2.3.3. Breakdown allocations

For each LFI radiometer we can express the system temperature as follows:

$$T_{\text{sys}} = T_{\text{Feed+OMT}} + T_{\text{FE}} + T_{\text{WG}s} + T_{\text{BE}}, \quad (8)$$

where the terms on the right hand side represent the contributions from the feed-horn/OMT, front-end module, waveguides and back-end module, respectively. Each of these terms can be expressed as:

$$T_{\text{Feed+OMT}} = (L_{\text{Feed}}L_{\text{OMT}} - 1)T_0$$

$$T_{\text{FE}} = L_{\text{Feed}}L_{\text{OMT}}T_{\text{FE}}^{\text{noise}}$$

$$T_{\text{WG}s} = \frac{L_{\text{Feed}}L_{\text{OMT}}(L_{\text{WG}s} - 1)T_{\text{eff}}}{G_{\text{FE}}}$$

$$T_{\text{BE}} = \frac{L_{\text{Feed}}L_{\text{OMT}}L_{\text{WG}s}T_{\text{BE}}^{\text{noise}}}{G_{\text{FE}}},$$

where T_0 is the physical temperature of the front-end; T_{eff} is an effective temperature which depends on the thermal design of the payload and radiometer interfaces; L_{Feed} and L_{OMT} are the insertion losses from the feed and OMT; $T_{\text{FE}}^{\text{noise}}$ and G_{FE} are the noise temperature and gain of the front-end module; $L_{\text{WG}s}$ is the insertion loss waveguide; $T_{\text{BE}}^{\text{noise}}$ is the back-end module noise temperature. In Table 2 we summarise the main LFI design allocations to the various elements contributing to the system temperature which have been set taking into account state-of-the-art technology.

2.4. Stability

Considering perturbations to ideal radiometer stability, the minimum detectable temperature variation of a coherent receiver is given by:

$$\delta T(f) = k_R T_{\text{sys}} \sqrt{\frac{1}{\tau \cdot \Delta\nu_{\text{eff}}} + \left[\frac{\delta G_T(f)}{G_T} \right]^2}, \quad (9)$$

where $\delta G_T(f)/G_T$ represents the contribution from amplifier gain and noise temperature fluctuations at post-detection sampling frequency f . HEMT amplifiers are known to exhibit significant $1/f$ noise, caused by the presence of traps in the semiconductor (Jarosik 1996), which would spoil the measurement if not suppressed. Amplifier fluctuations show a characteristic power spectral density $P(f) \propto 1/f^\alpha$ with $\alpha \approx 1$, so that the noise power spectral density is given by:

$$P(f) \approx \sigma^2 \left[1 + \left(\frac{f_k}{f} \right)^\alpha \right], \quad (10)$$

where σ^2 represents the white noise limit and the knee-frequency, f_k is the frequency at which the white noise and $1/f$ components give equal contributions to the power spectrum (see Meinhold et al. 2009 for a detailed discussion of the LFI noise properties).

The $1/f$ noise component not only degrades the sensitivity but it also introduces spurious correlations in the time ordered data and sky maps. The reference frequency to set a requirement on the knee frequency for LFI is the spacecraft spin frequency, 1 rpm, or 17 mHz. However, detailed analyses (Maino et al. 2002, Keihänen et al. 2004) have

shown that for the Planck scanning strategy a higher knee frequency ($f_k < 50$ mHz) is acceptable as robust destriping and map making algorithms can be successfully applied to suppress the effects of low-frequency fluctuations. Because a total power HEMT receiver would have typical knee frequencies of 10 to 100 Hz, a very efficient differential design is needed for LFI in order to meet the 50 mHz requirement.

2.5. Systematic effects

Throughout the design and development of LFI a key driver has been the minimisation and control of systematic effects, i.e., deviations from the signal that would be produced by an instrument with axially symmetric Gaussian beams, with ideal pointing and pure Gaussian white noise. These include optical effects (e.g., straylight, misalignment, beam distortions), instrument intrinsic effects (e.g., non-stationary and correlated noise features such as $1/f$ noise, spikes, glitches, etc.), thermal effects (e.g., temperature fluctuations in the front-end or other instrument interfaces), pointing errors. Dedicated analyses were required to evaluate the impact of instrument non-idealities on polarisation measurements. For LFI we set an ambitious upper limit to the global impact of systematic effects of $< 3 \mu\text{K}$ per pixel at the end of the mission and after data processing. A detailed discussion of the impact of various systematic effects in precision CMB anisotropy measurements can be found in Mennella et al. (2003).

The LFI receiver (discussed in Section 3) is designed with the primary objective of minimising the impact of $1/f$ noise, thermal fluctuations and non-ideal receiver components. After a description of the design solutions for the most critical LFI components and interfaces (Sections 4 to 7), in Sect. 8 we shall come back to a summary of the LFI systematic error budget to be compared with on-ground tests and in-flight performances.

3. Instrument concept

The heart of the LFI instrument is an array of 22 differential receivers based on cryogenic high-electron-mobility transistor (HEMT) amplifiers. Cooling of the front-end is achieved by a closed-cycle hydrogen sorption cooler (Morgante et al. 2009), with a cooling power of about 1 W at 20 K, which also provides 18 K pre-cooling to the HFI.

Radiation from the sky intercepted by the Planck telescope is coupled to 11 corrugated feed horns, each connected to a double-radiometer system, the so-called radiometer chain assembly (RCA, see Fig. 1). The complete LFI array, including 11 RCAs and 22 radiometers, is called radiometer array assembly (RAA).

3.1. Radiometric Chain Assemblies

Downstream of each feedhorn, an orthomode transducer (OMT) separates the signal into two orthogonal polarisations with minimal losses and cross-talk. Two parallel independent radiometers are connected to the output ports of the OMT, thus preserving the polarisation information. Each radiometer pair is split into a front-end module (FEM) and a back-end module (BEM) to minimise power dissipation in the actively cooled front-end. A set of composite waveguides connect the FEM and the BEM.

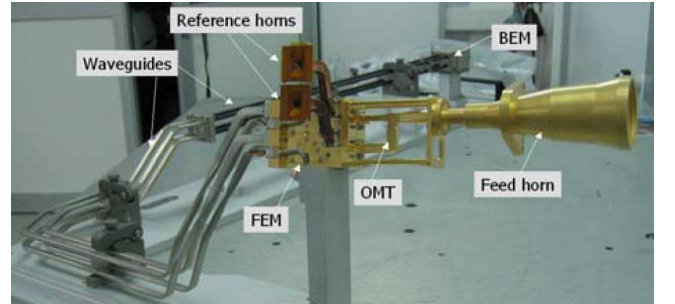
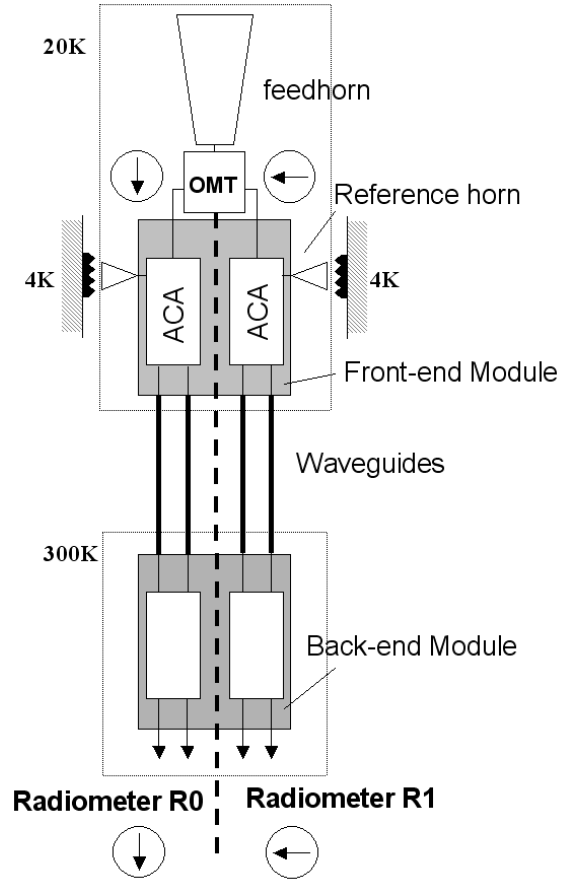


Fig. 1. Top: Schematic of a radiometer chain assembly (RCA). The LFI array has 11 RCAs, each comprising two radiometers carrying the two orthogonal polarisations. The RCA is constituted by a feed horn, an orthomode transducer (OMT), a front-end module (FEM) operated at 20 K, a set of four waveguides that connect FEM to the back-end module (BEM). The notations "0" and "1" for the two radiometers in the RCA denote the branches downstream the main and side arms of the OMT, respectively. Each amplifier chain assembly (ACA) comprises a cascaded amplifier and a phase switch. Bottom: picture of a 30 GHz RCA integrated before radiometer-level tests.

The stringent stability requirements are obtained with a pseudo-correlation receiver in which the signal from the sky is continuously compared with the signal from an internal blackbody reference load. The loads, one for each radiometer, are cooled to approximately 4 K by a Stirling cooler that provides the second pre-cooling stage for the HFI bolometers. Each receiver has two internal symmetric legs, so that each RCA comprises four waveguides and four detector diodes (Fig. 1).

3.2. Radiometer Array Assembly

A schematic of the Radiometer Array Assembly (RAA), is shown in Fig. 2. Each RCA has been integrated and tested separately, and then mounted on the RAA without de-integration to ensure stability of the radiometer characteristics after calibration at RCA level (Villa et al 2009b??).

A main frame supports the LFI 20 K front-end (with feeds, OMTs and FEMs) and interfaces the HFI 4 K front-end box in the central portion of the focal plane. The HFI 4 K box is linked to the 20 K LFI main frame with insulating struts, and provides the thermal and mechanical interface to the LFI reference loads. Forty-four waveguides connect the LFI front-end unit (FEU) to the back-end unit (BEU) which is mounted on the top panel of the Planck service module (SVM) and is maintained at a temperature of ~ 300 K. The BEU comprises the eleven BEMs and the data acquisition electronics (DAE) unit. After on-board processing, provided by the Radiometer Box Electronics Assembly (REBA), the compressed signal is down-linked to the ground station together with housekeeping data.

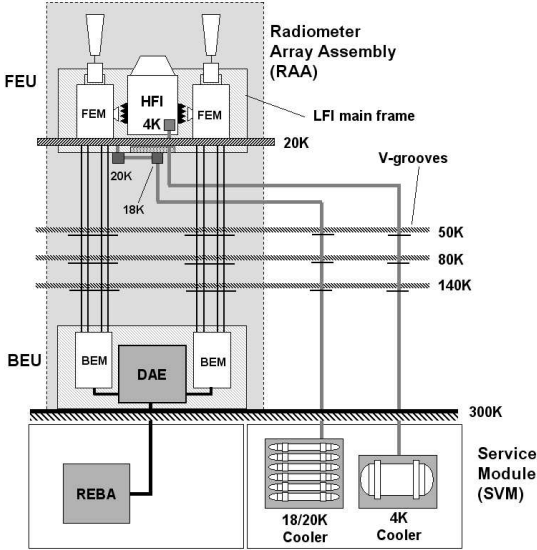


Fig. 2. Schematic of the LFI system displaying the main thermal interfaces with the V-grooves and connections with the 20 K and 4 K coolers. Two RCAs only are shown in this scheme. The Radiometer Array Assembly (RAA) is represented by the shaded area and comprises the FEU and BEU. The entire LFI RAA includes 11 RCAs, with 11 feeds, 22 radiometers, and 44 detectors.

A major design driver has been to ensure acceptable conductive and radiative parasitic thermal loads on the 20K stage, particularly those introduced by waveguides and cryo-harness. As we will discuss below, sophisticated design solutions were implemented for these units. In addition, three thermal sinks were used to largely reduce the parasitic loads in the 20K stage; these are the three conical shields (*V-grooves*) introduced in the Planck payload module (PPLM) to thermally decouple in the cold telescope enclosure, passively cooled to ~ 50 K, from the SVM at ~ 300 K (Tauber et al 2009a). The V-grooves also intercept parasitics from the coolers piping and HFI equip-

ment, and are expected to reach in-flight temperatures of approximately 140 K, 80 K and 50 K, respectively.

The FEU is aligned in the focal plane of the telescope and supported by a set of three thermally insulating bipods attached to the 50 K telescope structure. The back-end unit is fixed on top of the Planck service module, below the lower V-groove. In Fig. 3 we show a detailed drawing of the RAA, including an exploded view showing its main sub-assemblies and units. After integration the RAA was first tested in a dedicated cryo-facility (Terenzi et al 2009??) for instrument level tests (Fig. 4), and then inserted in the payload module after integration of the HFI 4 K box. Fig. 5 shows the LFI within the Planck satellite.

3.3. Receiver design

The LFI receivers are based on an additive correlation concept, or pseudo-correlation, analogous to schemes used in previous applications in early works (Blum 1959; Colvin 1961) as well as in recent CMB experiments (Staggs et al. (1996), WMAP). The LFI design introduces new features that optimise stability and immunity to systematics within the constraints imposed by cryogenic operation and by integration into a complex payload such as Planck. The FEM contains the most sensitive part of the receiver, where the pseudo-correlation scheme is implemented, while the BEM provides further RF amplification and detection.

In each radiometer (Fig. 6), after the OMT, the voltages of the signal from the sky horn, $x(t)$, and from the reference load, $y(t)$, are coupled to a 180° hybrid which yields the mixed signals $(x + y)/\sqrt{2}$ and $(x - y)/\sqrt{2}$ at its two output ports. These signals are then amplified by the cryogenic low noise amplifiers (LNAs) characterised by noise voltage, gain and phase n_{F1} , g_{F1} , ϕ_{F1} and n_{F2} , g_{F2} , ϕ_{F2} . One of the two signals then runs through a switch that applies a phase shift which oscillates between 0 and 180° at a frequency of 4096 Hz. A second phase switch is mounted for symmetry and redundancy on the other radiometer leg, but it does not introduce any switching phase shift. The signals are then recombined by a second 180° hybrid coupler, thus producing an output which is a sequence of signals proportional to $x(t)$ and $y(t)$ alternating at twice the phase switch frequency.

In the back-end modules (Fig. 6), the RF signals are further amplified in the two legs of the radiometers by room temperature amplifiers characterised by noise voltage, gain and phase n_{B1} , g_{B1} , ϕ_{B1} and n_{B2} , g_{B2} , ϕ_{B2} . The signals are then filtered and then detected by square-law detector diodes. A DC amplifier then boosts the signal output which is connected to the data acquisition electronics. The sky and reference load DC signals are integrated, digitised and then transmitted to the ground as two separated streams of sky and reference load data.

The sky and reference load signals recombined after the second hybrid in the FEM have highly correlated $1/f$ fluctuations. This is because, in each radiometer leg, they undergo the same instantaneous fluctuations in all the LNA stages. Furthermore, the fast modulation drastically reduces the impact of $1/f$ fluctuations coming from the back-end amplifiers and detector diodes, since the switch rate ~ 4 kHz is much higher than the $1/f$ knee frequency of the BEM components. By taking the difference between the DC

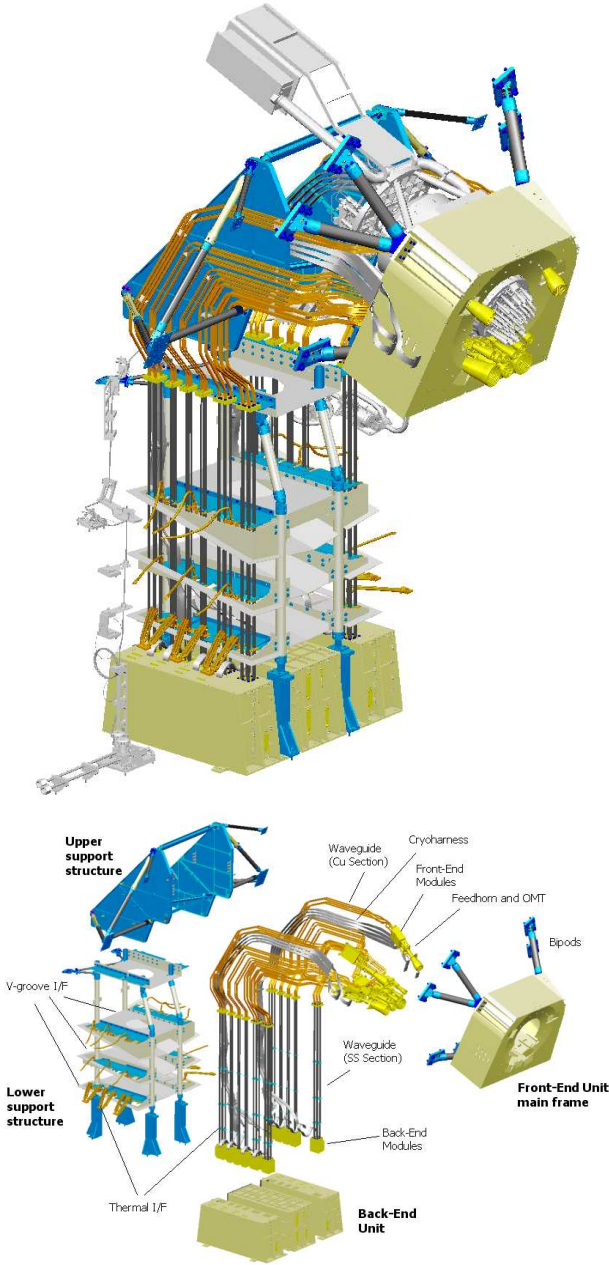


Fig. 3. LFI Radiometer Array Assembly (RAA). Top: drawing of the integrated instrument showing the focal plane unit, waveguide bundle and back-end unit. The elements that are not part of LFI hardware (HFI front-end, cooler pipes, thermal shields) are shown in light gray. Bottom: More details are visible in the exploded view, as indicated in the labels.

output voltages V_{sky} and V_{load} , therefore, the $1/f$ noise is highly reduced.

Differently from the WMAP receivers, the LFI phase switches and second hybrids have been placed in the front end. This allows full modularity of the FEMs, BEMs and waveguides, which in turns simplifies the integration and test procedure. Furthermore, this design does not require that the phase be preserved in the waveguides, a major advantage for the complex routing imposed by the LFI-HFI integration and for the potentially significant thermo-elastic effects from the cryogenic interfaces in the Planck payload.

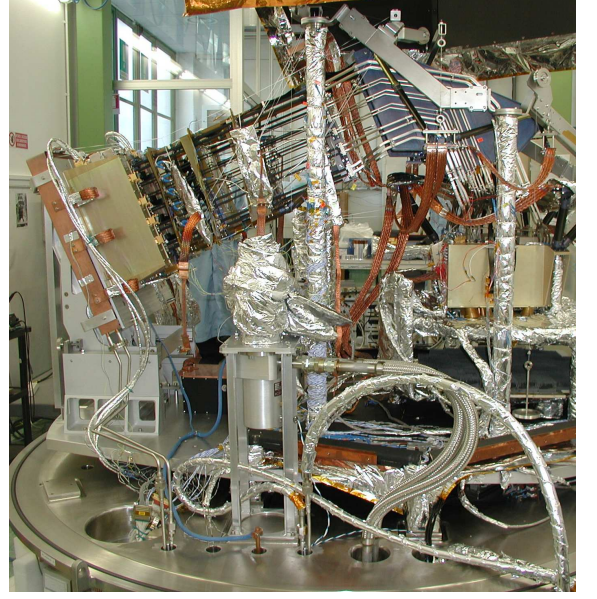


Fig. 4. The LFI instrument in the configuration for instrument level test cryogenic campaign.

In principle, for a null differential output corresponding to a perfectly balanced system, fluctuations would be fully suppressed in the differenced data. In practice, for LFI, a residual offset will be necessarily present due to input asymmetry between the sky arm (~ 2.7 K from the sky, plus ~ 1 K from the reflectors) and the reference load arm (with physical temperature ~ 4.5 K), plus a small contribution from inherent radiometer asymmetry. To compensate for this effect, a gain modulation factor r is introduced in software to null the output by taking the difference $\bar{p} = V_{\text{sky}} - r V_{\text{load}} \approx 0$. In the next section we will discuss the signal model in more detail.

3.3.1. Signal model

If $x(t)$ and $y(t)$ are the input voltages at each component, then the transfer functions for the hybrids, the front-end amplifiers, the phase switches and the back-end amplifiers can be written, respectively, as:

$$f_{\text{hybrid}} : \{x, y\} \rightarrow \left\{ \frac{x+y}{\sqrt{2}}, \frac{x-y}{\sqrt{2}} \right\} \quad (11)$$

$$f_{\text{amp}}^{\text{FE}} : \{x, y\} \rightarrow \{g_{F1}(x + n_{F1})e^{i\phi_{F1}}, g_{F2}(y + n_{F2})e^{i\phi_{F2}}\}$$

$$f_{\text{sw}} : \{x, y\} \rightarrow \{x, y\sqrt{A_j}e^{i\theta_j}\}, j = 1, 2$$

$$f_{\text{amp}}^{\text{BE}} : \{x, y\} \rightarrow \{g_{B1}(x + n_{B1})e^{i\phi_{B1}}, g_{B2}(y + n_{B2})e^{i\phi_{B2}}\},$$

where θ_1 and θ_2 represent the phase shifts in the two switch states (nominally, $\theta_1 = 0$ and $\theta_2 = 180^\circ$), A_1 and A_2 represent the fraction of the signal amplitudes that is transmitted after the phase switch in the two states (for a lossless switch $A_1 = A_2 = 1$). Based on these transfer functions and on the topology of the LFI receiver discussed above, we developed a detailed analytical description of the receiver and evaluated its susceptibility to systematic effects by studying the impact of deviation from ideal radiometer behaviour on the differenced output (Seiffert et al. 2002; Mennella et al. 2002a). In addition to the analytical treatment, a numeri-

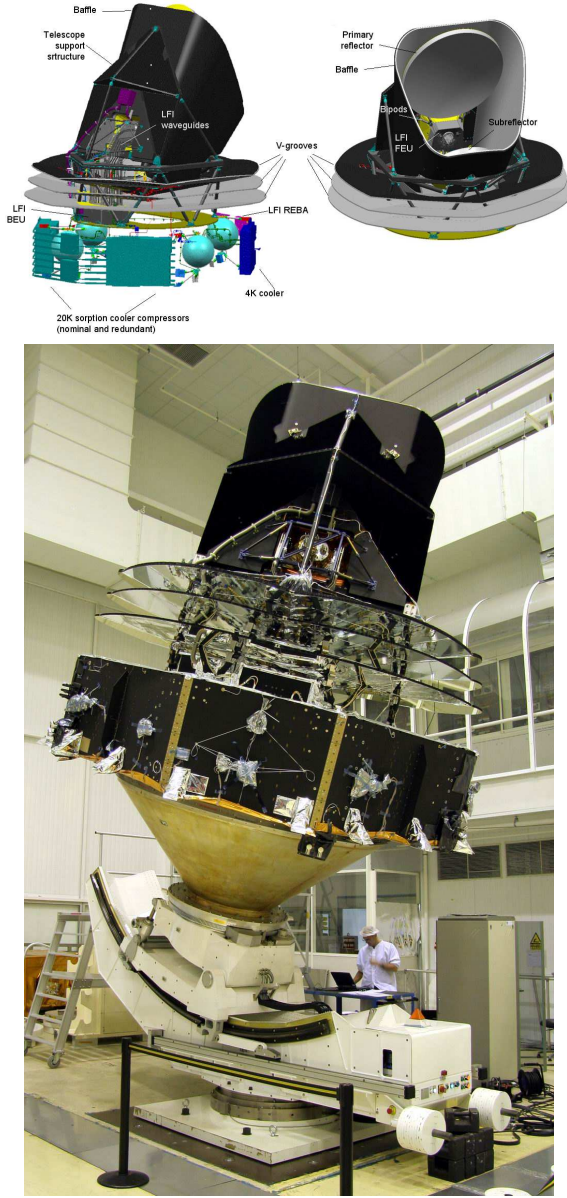


Fig. 5. Top: schematic of the Planck satellite showing the main interfaces with the LFI RAA on the spacecraft. Bottom: back view of Planck showing the RAA integrated on the PPLM. The LFI Back-end unit is the box below the lowest V-groove and resting on the top panel of the SVM.

cal model of the RCA signals has been developed (Battaglia et al. 2009).

For small phase mismatches and assuming negligible phase switch imbalance, the power output of the differenced signal after applying the gain modulation factor is given by:

$$\Delta p = a k \beta \left[\tilde{T}_{A,sky} (G - r I) - r \tilde{T}_{A,load} \left(G - \frac{1}{r} I \right) + (1 - r) T_{sys} \right], \quad (12)$$

where a is the proportionality constant of the square law detector diode, G and I are the effective power gain and

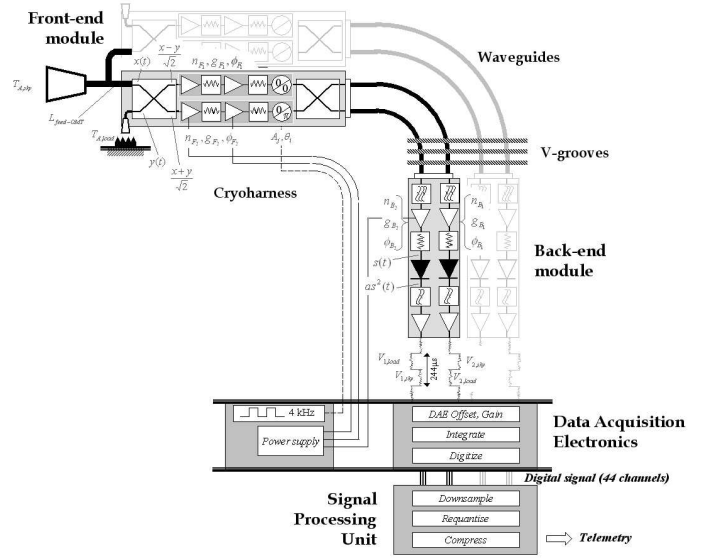


Fig. 6. LFI receiver scheme, shown in the layout of a Radiometer Chain Assembly (RCA). Some details in the receiver components (e.g., attenuators, filters, etc) differ slightly for the different frequency bands.

isolation of the system:

$$G \simeq \frac{1}{4} g_B^2 (g_{F1}^2 + g_{F2}^2 + 2g_{F1}g_{F2})$$

$$I \simeq \frac{1}{4} g_B^2 (g_{F1}^2 + g_{F2}^2 - 2g_{F1}g_{F2}), \quad (13)$$

where g_B is the voltage gain of the BEM in the considered channel. In Eq. (12) the temperature terms:

$$\tilde{T}_{sky} = \frac{T_{sky}}{L_{feed} L_{OMT}} + \left(1 - \frac{1}{L_{feed} L_{OMT}} \right) T_{phys}$$

$$\tilde{T}_{load} = \frac{T_{load}}{L_{4K}} + \left(1 - \frac{1}{L_{4K}} \right) T_{phys}, \quad (14)$$

represent the sky and reference load signals at the input of the first hybrid, where L_{4K} is the insertion loss of the reference horn, and $T_{phys} \simeq 20$ K is the front-end physical temperature.

Fig. 7. Curves of equal f_k (in Hz) on the plane T_y (K, thermodynamic temperature), T_n assuming thermodynamic sky temperature of 2.7 K. Each panel refers to a different frequency channel. The dashed contour refers to values for which the knee frequency is equal to the spin frequency ($f_{spin} = 0.0166$ Hz). The graphs also show the range of typical LFI noise temperature values (grey area) and the nominal reference load temperature (4 K - double horizontal line).

3.3.2. Knee frequency and gain modulation factor

For a system with good isolation (>13 dB), as expected in a well matched system, from Eq. (12) it is easy to see that the power output is nulled for

$$r = \frac{\tilde{T}_{\text{sky}} + T_{\text{noise}}}{\tilde{T}_{\text{load}} + T_{\text{noise}}}. \quad (15)$$

In this case the gain fluctuations are fully suppressed and the radiometer is sensitive only to the $1/f$ noise caused by noise temperature fluctuations, which represents only a small fraction of the amplifiers instability. For an optimal choice of the gain modulation factor, the resulting knee frequency is given by:

$$f_k \simeq \Delta\nu \left(\frac{A(1-r)T_{\text{sys}}}{T_{\text{sky}} + T_{\text{sys}}} \right)^2 \propto (1-r)^2. \quad (16)$$

Thus, in principle, for small input offsets $\tilde{T}_{\text{sky}} \simeq \tilde{T}_{\text{load}}$ very small knee frequencies can be obtained. Fig. 7 displays expected knee frequencies for parameters typical of the LFI channels as a function of noise temperature and reference load temperature, assuming ideal gain and phase match. Note that for $T_{\text{load}} \approx 4$ K we expect f_k an order of magnitude lower than for $T_{\text{load}} \approx 20$ K. This was the driver for implementing reference loads at 4K at the cost of some complexity in the thermo-mechanical interfaces in the focal plane. It can also be shown (Mennella & Bersanelli 2001) that the same value of r that minimises the radiometer sensitivity to $1/f$ noise is also effective in reducing the susceptibility to other systematic effects such as back-end temperature variations.

It is essential that the gain modulation factor r be calculated with sufficient precision to reach the required stability. Simulations and testing show that the needed accuracy that ranges from $\pm 1\%$ (30 GHz) to $\pm 0.5\%$ (70 GHz). This accuracy can be obtained with different methods (Mennella et al. 2002), the simplest being to evaluate the ratio of the total power output voltages averaged over a suitable time interval, $r \simeq \bar{V}_{\text{sky}}/\bar{V}_{\text{load}}$. In Fig. 8 we show, as an example, the data streams from one of the 44 LFI detectors with the two total power signals and differenced data. The LFI telemetry specifications ensure that the total power data from both the sky and reference load samples will be downloaded, so calculation of r and differencing will be performed on the ground.

Further suppression of common fluctuation modes, typically of thermal or electrical origin, is obtained by taking the noise-weighted average of the two detectors associated to each radiometer (see Appendix A in Mennella et al 2009) as well as in the differencing of the main and side arm radiometers signals when analysing data for polarisation (Leahy et al. 2009).

3.3.3. Noise temperature

The LFI radiometer sensitivity is essentially independent of the temperature of the reference loads. From Eq. (12) it follows that, to first order, the radiometer sensitivity is:

$$\delta T = \sqrt{\frac{2}{\tau \cdot \Delta\nu}} (T_{\text{sys}} + T_{\text{sky}}) \sqrt{1 + \eta_L}, \quad (17)$$

where

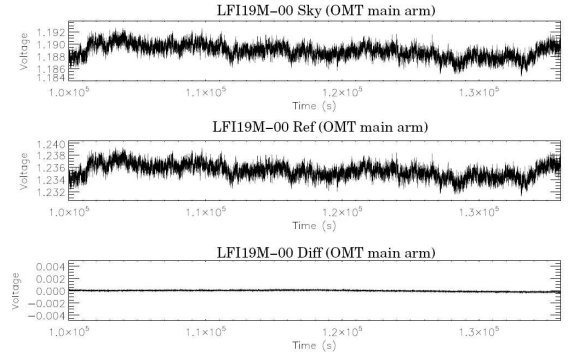


Fig. 8. Example of uncalibrated data stream from one of the 44 LFI detectors (LFI19M-00, at 70 GHz) recorded during instrument level tests. The upper and middle panels show the data for the sky and reference load inputs, while the lower panel shows differenced data stream with optimal gain modulation factor.

$$\eta_L = \frac{(T_{N,B}/G_F)^2}{(T_{\text{sys}} + T_{\text{sky}})(T_{\text{sys}} + T_{\text{load}})}, \quad (18)$$

and $T_{N,B}$ is the noise temperature of the back-end, G_F is the gain of the front end. For parameter values typical of LFI we have $\eta_L < 10^{-3}$, so that the dependence of the noise temperature on T_{load} is extremely weak. The advantage of cooling the reference load to 4 K, therefore, rests solely on better suppression of systematics, not on sensitivity.

4. LFI configuration and subsystems

The overall LFI system is shown schematically in Fig. 9. In this section we provide an overview of the instrument units and main subsystems. Details on the development of the most critical hardware components are given in companion papers that will be referenced below.

4.1. The Front-End Unit

4.1.1. Focal plane design

The disposition of the LFI feeds in the focal plane is driven by optimisation of angular resolution and of recovery of polarisation information. In addition, requirements on proper sampling of the sky and rejection of crosstalk effects need to be met.

The central portion of the Planck focal plane is occupied by the HFI front end, as higher frequency channels are more susceptible to optical aberration. The LFI feeds are located as close as possible to the focal plane centre compatible with mechanical interfaces with HFI and 4 K reference loads (Fig. 10). Miniaturised designs for the FEMs and OMT are implemented to allow optimal use of the focal area. The 70 GHz feeds, most critical for cosmological science, are placed in the best location for angular resolution and low beam distortion required for this frequency (Sandri et al. 2009).

A key criterion for the feed arrangement is that the E and H planes as projected in the sky will allow optimal discrimination of the Stokes Q and U parameters. The polarisation information is obtained by differencing the signal measured by the X and Y radiometers in each RCA, which



Optical simulations as well as extensive testing have been performed to evaluate the tolerance of mutual obscuration between nearby feeds in the focal plane (D’Arcangelo et al. 2003), both internal to LFI and between LFI and HFI. The results show that to avoid any significant effects each feed field of view must be within an angle of $\sim 45^\circ$ from the edge of the horn aperture. The focal plane design meets this requirement.

$\theta_{\text{FWHM}} \simeq 13'$ at 70 GHz, we have $\Delta\phi_{\text{scan}} < \theta_{\text{FWHM}}/3$ and the Nyquist criterion for sky sampling is comfortably met.

The LFI main frame provides thermo-mechanical support to the LFI radiometer front-end, but it also supports the HFI and interfaces to the cold end (nominal and redundant) of the 20 K sorption cooler. In fact, some of the key requirements on the LFI mainframe (stiffness, thermal decoupling, optical alignment) are driven by the HFI rather than the LFI instrument. A detailed analysis was carried out to identify appropriate materials for the main frame, which is built in Aluminum alloy 6061. Three dismountable sub-units facilitate integration of the complete RCAs and of the HFI.

The interface of the FPU towards the 50 K payload module structure must ensure thermal decoupling as well as compliance with eigenfrequencies from lift off loads. A trade-off was made to identify the proper material properties, fibre orientations, and strut inclinations. The chosen configuration was a set of three 225-mm-long CFRP T300 bipods, inclined at 50°. The LFI-HFI interface is provided

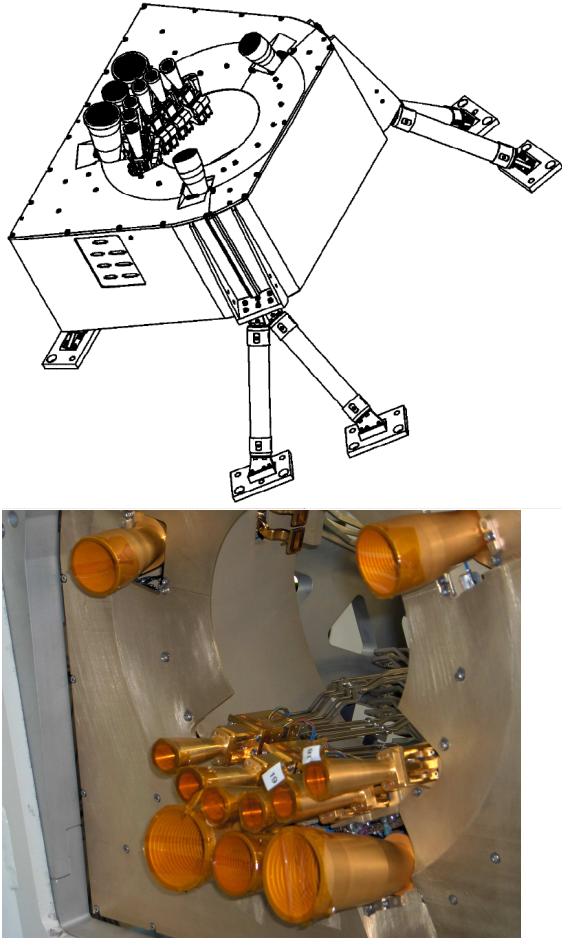


Fig. 10. Arrangement of the LFI feeds in the focal plane. Top: mechanical drawing of the main frame and focal plane elements. Shown are the bipods connecting the FPU to the telescope structure. Bottom: picture of the LFI flight model focal plane.

by a structural ring connected to the HFI by six insulating struts locked to the LFI main frame through a shaped flange. The design of the interface ring allows HFI integration inside the LFI as well as waveguide paths, while ensuring accurate alignment of the reference loads with the reference horns mounted on the FEMs.

4.1.3. Feed horns

The LFI feeds require highly symmetry beams, low levels of side lobes (-35dB), cross-polarisation (-30dB) and return loss (-25dB), as well as good control of the phase centre location (Villa et al. 2002). Dual profiled conical corrugated horns have been designed to meet all these compelling requirements, a solution that has the further advantage of high compactness and design flexibility. The profiles are composed by a sine squared inner section (i.e., with horn section $R(z) \propto \sin^2(z)$) and by an exponential outer section ($R(z) \propto \exp(z)$).

The detailed electromagnetic designs of the feeds were developed based on the entire optical configuration of the feed-telescope system. The control of the edge taper only required minimal changes on the feed aperture and overall feed sizes, so that an iterative design process could be carried out at system level.

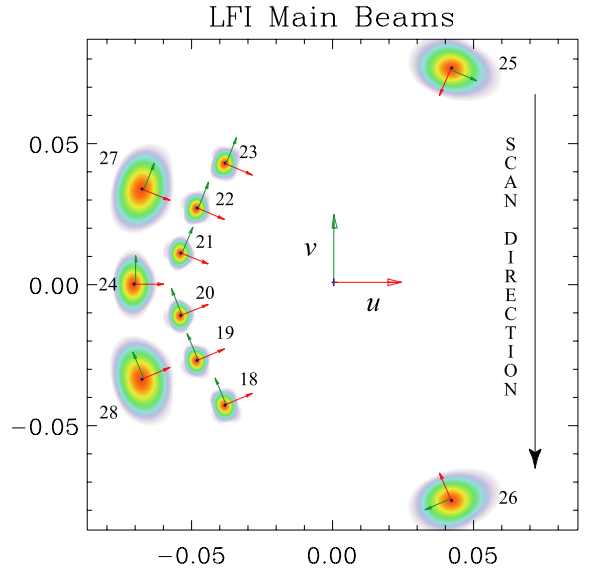


Fig. 11. Footprint of the LFI main beams on the sky and polarisation angles as seen by an observer looking towards the satellite along its optical axis ((u, v) plane, see Sandri et al. 2009 for details). Labels from 18 to 23 refer to 70 GHz horns, from 24 to 26 refer to 44 GHz horns, and 27 and 28 refer to 30GHz horns. The scan direction, orthogonal to the focal plane symmetry axis, is indicated by an arrow. All the relative angles in pairs of feeds aligned along the scan direction are shifted by 45° , with the exception of RCA24.

The evaluation of straylight effects in the optimisation process required extensive simulations (carried out with GRASP8 software) of the feed-telescope assembly for several different feed designs, edge tapers, and representative position in the focal plane (Sandri et al. 2009). A multi-GTD approach was necessary since the effect of shields and multiple scatter needed to be included in the simulations. In Table 3 we report the main requirements and characteristics of the LFI feed horns. The details of the design, manufacturing, and testing of the LFI feed horns are discussed in Villa et al. (2009).

Table 3. Baseline specifications of the LFI feed horns (the insertion loss is referred at 20 K).

	30 GHz	44 GHz	70 GHz
Band [GHz]	27-33	39.6-48.4	63-77
Return Loss	<-25 dB	<-25 dB	<-25 dB
Insertion Loss	<0.1 dB	<0.1 dB	<0.1 dB
Edge Taper (at 22°)	30 dB	30 dB	25 dB
Side Lobes	<-35 dB	<-35 dB	<-35 dB
Cross polarisation	<-30dB	<-30dB	<-30dB

4.1.4. Orthomode transducers

The use of orthomode transducers (OMTs) allows the full power intercepted by the feed horns to be used by the LFI radiometers, and makes each receiver intrinsically sensitive to linear polarization. The OMT splits the TE_{11} signal from the output circular waveguide of the feed horn into two orthogonal polarised components. Low insertion loss

(< 0.15dB) is needed to minimise impact on radiometer sensitivity. In addition, OMTs are critical components for achieving the ambitious wide bandwidth specification, especially when combined to the miniaturization imposed by the focal plane arrangement.

Table 4. Baseline specifications of the LFI orthomode transducers (the quoted insertion loss is at 20 K)

	30 GHz	44 GHz	70 GHz
Band [GHz]	27-33	39.6-48.4	63-77
Isolation	<-40 dB	<-40 dB	<-40 dB
Return Loss	<-20 dB	<-20 dB	<-20 dB
Insertion Loss	<0.15 dB	<0.15 dB	<0.15 dB
Cross polarisation	<-25dB	<-20dB	<-20dB

These requirements made commercial OMTs inadequate for LFI, and a dedicated design development was carried out for these components (Villa et al. 2009b). An asymmetric design was selected, with a common polarisation section connected to the feed horn and a main and side arms in which the two polarisations are separated. A modular design approach was developed, in which six different sections were identified, each corresponding to a specific electromagnetic function. While the basic configuration of the OMTs at different frequencies is scaled from a common design, some details are optimised depending on frequency, such as the location of the waveguide twist in the side arm or in the main arm. The main design specifications for the LFI orthomode transducers are given in Table 4. Detailed discussion of the design, manufacturing and unit-level testing of the LFI OMTs are reported in (Villa et al. 2009b).

4.1.5. Front-end modules

The performances of the LFI rely largely on its front-end modules (FEMs, see Table ??). Detailed descriptions of the LFI 30 GHz and 44 GHz FEMs are given by Davis et al. (2009), and of the 70 GHz FEMs by Varis et al. (2009).

Each FEM accepts four input signals, two from the rectangular waveguide outputs of the OMT and two from the external reference loads viewed by rectangular horns attached to the FEMs (Fig. 6).

In each half-FEM, the sky and reference input signals are connected to a hybrid coupler (or “magic-T”). To minimise front-end losses, waveguide couplers were used, machined in the aluminium alloy FEM body and gold-plated. At 20 K the front-end hybrid is estimated to contribute 0.1 to 0.2 dB to the system noise. The first hybrid divides the signals between two waveguide outputs along which the low noise amplifiers and phase shifters are mounted. The internal waveguide design ensures that the phase is preserved at the input of the second hybrid. The signals are thus recombined at the FEM outputs as voltages proportional to the sky or reference load signal amplitude, depending on the state of the modulated phase switches.

At 70 GHz the large number of channels called for a highly modular FEM design, where each half-module could be easily dismantled and replaced. In addition, the element hosting the LNAs and the phase shifters (the so called amplifier chain assembly, ACA, see Fig. 1) are built as separable units. This allowed high flexibility during selection and



Fig. 12. Picture of nine of the eleven feed horns and associated OMTs, FEMs and waveguides before integration of the HFI front end. The six smaller feeds in the front are the 70 GHz channels, while in the back row are the two 30 GHz feeds and one of the 44 GHz feeds in the middle. Visible are part of the twisted Cu waveguide sections. The reference horns are visible (protected by a kapton layer): for the 70 GHz FEMs they are embodied in the FEMs, while for the 30 and 44 GHz they are flared waveguide sections.

testing, which proved extremely useful when replacement with a spare unit was required in an advanced stage of integration (see Mennella et al. (2009)). At 30 and 44 GHz, a multi-splitblock solution was devised to facilitate testing and integration, in which the four ACAs were mounted to end-plates and arranged in a mirror-image format.

LNAs. In order to meet LFI requirements it was necessary to reach amplifier noise temperatures lower than previously achieved with multi-stage transistor amplifiers. We implemented state-of-the art cryogenic Indium Phosphide (InP) HEMT technology at all frequencies. Each front-end LNA needs to provide a minimum of 30 dB of gain to reject back-end noise, which required 4 to 5 stage amplifiers. In addition to low noise, the InP technology enables very low power operation, which is essential to meet the requirements for heat load at 20 K. The amplifiers were selected and tuned for best operation at low drain voltages and for gain and phase match between paired radiometer legs, which is crucial for good balance.

The 70 GHz receivers are based on monolithic microwave integrated circuit (MMIC) semiconductors (Fig. 14) while at 30 and 44 GHz discrete HEMTs on a substrate (MIC technology) are used. To reach lowest possible noise temperatures, ultra-short gate devices are adopted. The final design used 0.1 μm gate length InP HEMTs man-

ufactured by TRW (now NGST) from the Cryogenic HEMT Optimisation Program (CHOP).

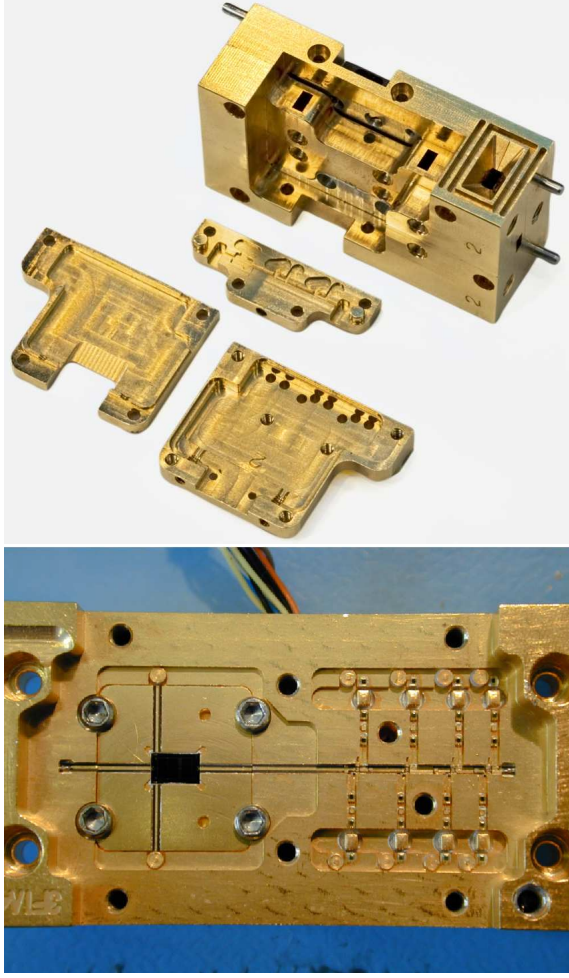


Fig. 13. Top: Structure of a 70 GHz half-FEM. On the top-right side of the module the reference horn antenna to couple the 4 K reference load is visible, surrounded by quarter-wave grooves. The parts supporting the amplifier chain assembly are dismantled and shown in the front. Bottom: picture of LNA and phase switch within a 30 GHz FEM. The RF channel incorporating the four transistors runs horizontally in this view. The phase switch is the black rectangular element on the left.

Phase shifters. After amplification the LNA output signals are applied to two identical phase shifters whose state is set by a digital control line modulated at 4 kHz. The signal is then conveyed via stripline to waveguide transitions to the second hybrid and then to the interface with the interconnecting waveguide assembly to the BEMs. The phase switch design used at all frequencies is based on a double hybrid ring configuration (Hoyland 2003). The switches, manufactured with InP PIN diodes, demonstrated excellent cryogenic performances for low $1/f$ noise contribution and good 180° phase shift capability and amplitude balance.

Electrical connections. Each of the 11 FEMs uses 16 to 20 low noise transistors and 8 phase switch diodes, all oper-

ated in cryo conditions. This sets demanding requirements in the design of the bias circuitry. The LNA biases are controlled by the data acquisition electronics (DAE) to obtain the required amplification and lowest noise operation. Different details in the design of the FEMs at each frequency minimise the number of supply lines. In the 30 and 44 GHz FEMs potentiometers were used to common most of the control wires. The cryo-harness wiring that connects the FEMs to the power supply is ~ 1.5 m of length (see Section 6.1), which requires that each wire is terminated in the FEM with electrical protection devices to avoid sharp spikes.

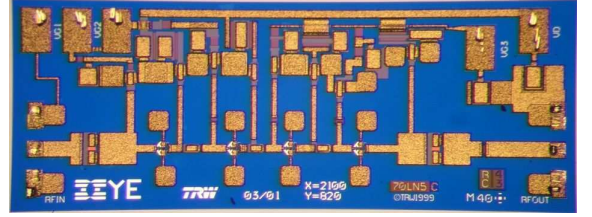


Fig. 14. A 4-stage Indium Phosphide HEMT MMIC low noise amplifier used in a flight model FEM at 70 GHz. The size of the MMIC is $2.1 \text{ mm} \times 0.8 \text{ mm}$.

Proper tuning of the LNAs is critical for best performances. Each front-end InP LNA is composed by 4 stages of amplification at 30 and 70 GHz and 5 stages at 44 GHz. The LNAs are driven by three voltages: a common drain voltage (V_d), a gate voltage for the first stage (V_{g1}) and a common gate voltage for the remaining stages (V_{g2}) (Fig. 15). The voltages V_{g1} and V_{g2} are programmable and are optimised in the tuning phase (Cuttaia et al. 2009). The total drain current, I_d flowing in the ACA is measured and is available in the instrument housekeeping.

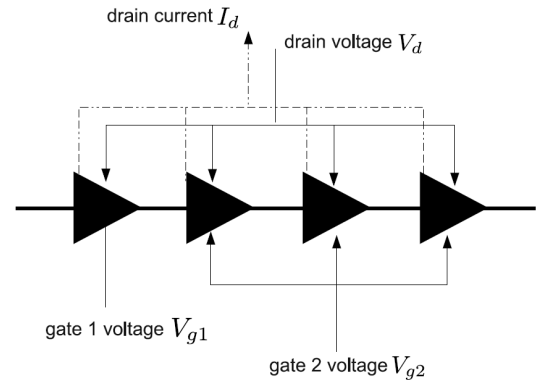


Fig. 15. DAE biasing to a front-end LNA. Each LNA is composed by four to five amplifier stages driven by a common drain voltage, a dedicated gate voltage to the first stage (most critical for noise performances) and a common gate voltage to the other stages.

4.2. The 4 K reference load system

Blackbody loads provide stable internal signals for the pseudo-correlation receivers (Valenziano et al. 2009).

Cooling the loads as close as possible to the ~ 3 K sky temperature minimises the radiometer knee frequency (Eq. (16)) and reduces the susceptibility to thermal fluctuations and to other systematic effects. Requirements are thus derived for the loads absolute temperature, $T_{4K} < 5$ K, as well as for the insertion loss of the reference horn, $L_{4K} < 0.15$ dB.

Connecting the loads to the HFI 4 K stage imposes challenging thermo-mechanical requirements on the system. The loads must be thermally disconnected from the reference horns feeding the 20 K FEMs. Complete decoupling is obtained by leaving a ~ 1.5 mm gap between the loads and the reference horns.

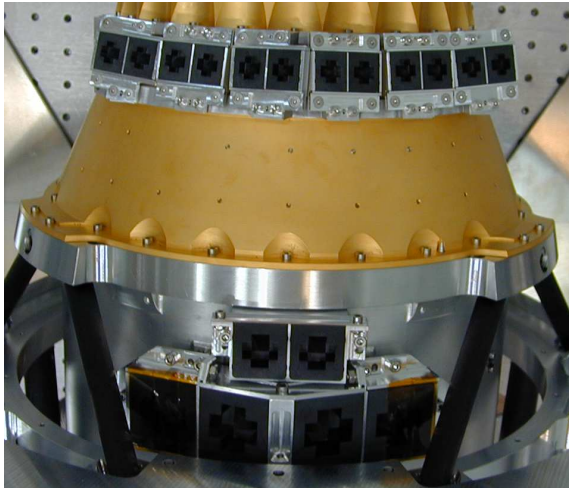


Fig. 16. Picture of the reference loads mounted on the HFI 4 K box. On the top is the series of loads serving the 70 GHz radiometers, while in the lower portion are the loads of the two 30 GHz FEMs and one of the 44 GHz FEMs. Note that each FEM is associated to two loads, each feeding a radiometer in the RCA.

Radiometric requirements for the loads were derived by analysis and tests (Valenziano et al 2009). The coupling between the reference horns and the loads are optimized to reduce reflectivity and to avoid straylight radiation leaking through the gap, with a required match at the horn aperture > 20 dB. For the 70 GHz radiometers the reference horns are machined as part of the FEM body, while for the 30 and 44 GHz they are fabricated as independent waveguide components and mounted on the FEM (Fig. 12). This is because of the different paths required to reach the loads, whose location on the 4K box is constrained by the LFI-HFI interface.

The loads configuration is the result of a complex trade-off between RF performances and a number of constraints such as allowed mass, acceptable thermal load on the 4 K stage, available volume. The latter is limited by the optical requirement of placing the sky horns close to the focal plane centre. In addition, the precise location and alignment of the loads on the HFI box need to follow the non-trivial orientation and arrangement of the FEMs, dictated by the optical requirements for angular resolution and polarisation. The final design comprises a front layer (made in ECR-110) shaped for optimal match with the reference

horn radiation pattern, and a back layer (ECR-117) providing excellent absorption efficiency.

Requirements on thermal stability at the 4K shield interface were set to $10\mu K\sqrt{s}$, i.e., at the same level as the HFI internal requirement. The 70 GHz loads are located in the top of the HFI 4 K box and the 30 and 44 GHz loads in the lower part (Fig. 12 and Fig. 16). Due to the position of the PID system on the HFI 4 K box (Lamarre et al 2009), this results in a more stable signal for the LFI 70 GHz loads than for the 30 and 44 GHz ones.

4.3. Waveguides

A total of 44 waveguides connect the 20 K FEU and the 300 K BEU through a length of 1.5 to 1.9 m, depending on RCA. Conflicting constraints of thermal, electromagnetic and mechanical nature imposed challenging trade-offs in the design. The LFI waveguides must ensure good thermal decoupling between the FEM and the BEM, while avoiding excessive attenuation of the signal. In addition, their mechanical structure must comply with the launch vibration loads. The asymmetric location of the FEMs in the focal plane, and the need to ensure integrability of the HFI in the LFI main frame as well as of the RAA on the spacecraft, impose complex routing with several twists and bends, which required a dedicated design for each individual guide.

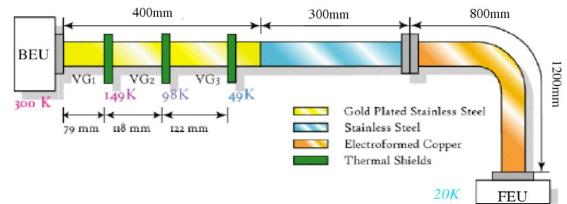


Fig. 17. Schematic of the LFI composite waveguide design, showing representative dimensions of the various sections as described in the text.

Table 6. RF requirements of the LFI waveguides.

	30 GHz	44 GHz	70 GHz
Insertion loss (20 K)	< 2.5 dB	< 3 dB	< 5 dB
Return loss	< 25 dB	< 25 dB	< 25 dB
Isolation	> 30 dB	> 30 dB	> 30 dB
Standard WG	WR28	WR22	WR12
Internal section (mm)	7.112×3.556	5.690×2.840	3.099×1.594

A composite configuration was devised with two separated sections: a stainless steel (SS) straight section connecting to the BEMs, and a Copper (Cu) section incorporating all the twists and bends and connecting to the FEMs (Fig. 17). The two sections are connected via custom-designed multiple flanges, each serving the four guides in each RCA.

All 44 SS sections have the same length (70 cm) and are gold-plated ($2\mu m$ thickness) in the first 40 cm near the BEM interface to minimise ohmic losses. They support es-

entially the entire 20K–300K thermal gradient. They are thermally sunk to the three V-grooves (Fig. 18) and their outer surfaces are black painted (Aeroglaze Z306) to optimise heat radiation.

The Cu sections, of lengths 80 to 120 cm depending on RCA, operate at a nearly constant temperature of 20 K, and are individually designed based on optimization of return loss compatible with the required routing. Precise criteria for the curvature radii, twist length and mechanical tolerances were followed in the design (D’Arcangelo et al. 2009). Dynamical analysis showed the need of two dedicated mechanical support structures to ensure compliance with the vibration loads of the Ariane V launch (Fig. 18).

The selected design proved to meet simultaneously the heat load limits to the 20 K stage (250 mW for the bundle of 44 guides) and the insertion loss at a level of few dBs. A thermal model was developed to calculate the temperature profile along the waveguide and the final solution was found using an analytical model.

The complex waveguide configuration, test modularity, and thermo-elastic considerations led to the choice of not requiring phase-matching through paired waveguides, which would have lead to a much more complex routing. The direct implication of this choice is that the phase switch modulation must be performed in the front-end part of the instrument which therefore required the implementation of phase switches with high performances (low insertion loss, good phase and amplitude match) at cryogenic temperatures.

D’Arcangelo et al. (2009) gives a full account of the manufacturing, qualification, and of the challenging test plan of the LFI waveguides.

4.4. Back-end unit

4.4.1. Back-end modules

The back-end modules (BEMs) are housed in the LFI back-end unit together with the DAE and are operated at room temperature ~ 300 K. Each BEM has four branches, coupled in pairs (Fig. 6). In each channel within the BEM the incoming signal is filtered by a band-pass filter, amplified by cascaded transistor amplifiers, detected by a detector diode, and DC-amplified. The BEM casing also incorporates bias and protection circuits and connectors. Room temperature noise figures < 3 dB and an overall amplification of 20 to 25 dB, depending on RCA, are specified for the BEM channels. Amplifier and detector diode instabilities are efficiently removed by the 4 kHz phase switching, so that amplifier knee frequencies of order 100 Hz are acceptable.

Amplifiers. The 30 and 44 GHz BEMs (Artal et al. 2009) use MMIC Gallium Arsenide (GaAs) amplifiers. Each LNA consists of two cascaded stages. The 30 GHz MMICs are commercial circuits using four stages of pseudomorphic HEMT with an operating bandwidth from 24 to 36 GHz, 23 dB of gain and 3 dB of noise figure. The 44 GHz MMICs were manufactured with a process employing a $0.2 \mu\text{m}$ gate length P-HEMT on GaAs. The 70 GHz BEMs (Varis et al. 2009) use the same type of Indium Phosphide MMIC amplifiers as in the FEMs. Although not required for perfor-

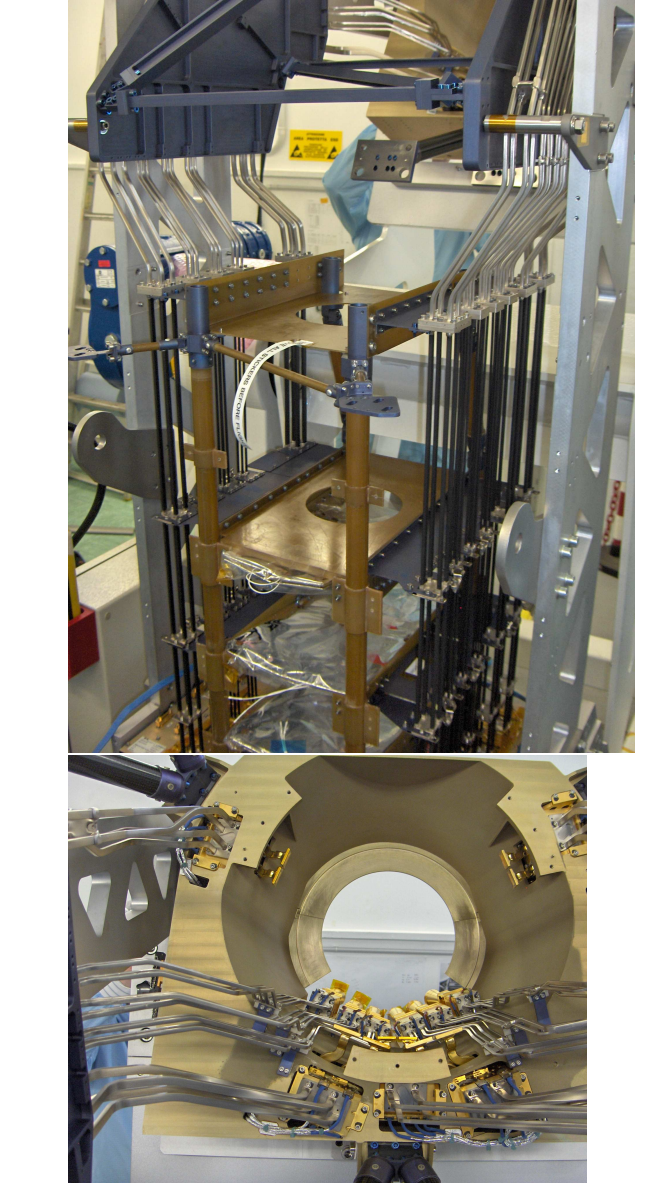


Fig. 18. Pictures of the LFI waveguides mounted on the RAA during the integration of the LFI flight model. Top: a view of the straight SS sections, black-painted on the outside and arranged in groups of four. On the upper part the Cu sections are connected through multiple flanges. Visible are also the upper and lower mechanical support structures. The three interface levels corresponding to the three V-grooves are also shown. Bottom: back view of the LFI front-end unit showing the twisted Cu sections connecting to the FEMs. The waveguide routing and central hole in the main frame are designed to interface with the HFI front-end 4 K box.

mance or power dissipation constraints, this solution proved convenient in conjunction with the FEM development.

Band pass filters. Band pass filters in the BEMs are used to define the bandwidth and to reject out-of-band parasitic signals. In the 30 and 44 GHz units the filter is based on microstrip coupled line structure which inherently provides band pass characteristics. Waveguide filters are instead adopted at 70 GHz, where the wavelength-scales cavity leads to acceptable size.

Detector diodes The detector design at 30 and 44 GHz uses commercially available GaAs planar doped barrier Schottky diodes. The diodes are mounted with a coplanar-to-microstrip transition to facilitate on-wafer testing prior of integration in the BEM. As in the FEM design, at 70 GHz the filters and the amplifier-detector assemblies of paired channels were mounted on separable modules to offer higher flexibility in the testing and optimisation phases.

DC amplifiers The detector diode is followed by a low noise DC-amp with a voltage gain adequate to the required analogue output voltage range for the DAE interface. In order to meet EMC requirements and grounding integrity the output voltages are provided as differential signals.

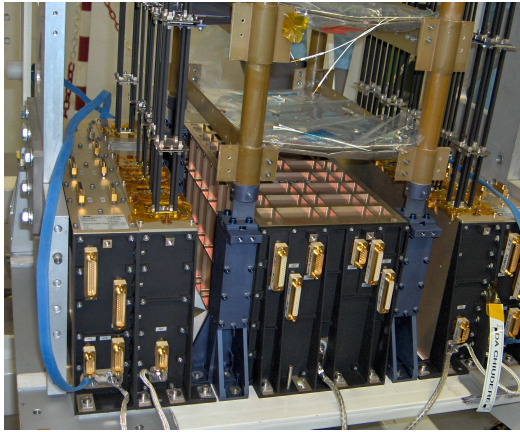


Fig. 19. Picture of the lower part of the LFI RAA during an advanced phase of the instrument FM integration showing the LFI back-end unit. The two lateral trays hosting the radiometer BEMs are symmetrically disposed to the left and right sides of the DAE-BEU box. Visible are the lower part of the straight SS waveguides.

4.4.2. Data acquisition electronics

The acquisition and conditioning of the science signals from the BEMs and of housekeeping data is performed by the data acquisition electronics. The DAE also provides power supply, conditioning and distribution to the RAA, and in particular DC biasing to the LNAs and phase switches in the FEMs, as well as to the BEM amplifiers. The DAE tags the acquired data using the information of its on-board time to ensure that correlation can be made on ground for proper pointing reconstruction. The raw data are then transmitted to the science processing unit for on-board processing.

As shown schematically in Fig. 9, the DAE functions are distributed into different sub-units. The “DAE-BEU box” and the “lateral trays” incorporate all the main functions, and are located in the back-end unit together with the radiometer BEMs (Fig. 19). A separated “DAE power box” is interfaced with the spacecraft in order to receive the primary power supply and generate the secondary voltages needed to the DAE.

The DAE-BEU box is in charge of conditioning and acquiring the science data. The signals coming from the 44 detectors are integrated and held during the synchronous

sampling and conversion. Science signals are digitised with 14-bit analogue-to-digital converters. There are 11 independent analogue acquisition chains, one for each RCA. In order to optimise the analog signals from the BEMs to the ADC dynamic range (-2.5 to 2.5 V), dedicated circuits remove an offset and then apply an amplification to the DC signal. Both offset and gain are programmable and are optimised as part of the instrument calibration process (Cuttaia et al. 2009; Mennella et al. 2009). Acquired data are converted into serial streams and automatically transferred to the signal processing unit in the REBA through synchronous serial links for processing and compression (Sect. 4.4.3).

The two DAE “lateral trays” contain the circuitry needed to provide the power supply to the RCAs, divided in four power groups (Fig. 9). These power supplies are independent from each other to minimise crosstalk and interference. The bias of each FEM and the controls for the phase switches are regulated to selectable voltage levels and filtered to achieve a minimum level of conducted noise. Particularly critical for the instrument performance is the optimal biasing of the FEM amplifiers. As described in Sect. 4.1.5, the bias voltages of the first LNA stage and of the following stages are separately programmable.

4.4.3. Radiometer electronics box (REBA)

Downstream the DAE, the LFI signals are digitally processed by the REBA (radiometer electronics box assembly), which also provides power supply and interface with the satellite SVM. The electronics hardware and on-board software are discussed by Rebolo et al. (2009). The REBA is a fully redundant unit and it is internally separated in different sub-units as schematically shown in Fig. 9.

The signal processing unit (SPU) receives the raw digital science data from the DAE and performs basic data reduction, data compression and science telemetry packetisation. The need to reject $1/f$ noise led to raw data sampling at 8192 Hz (or $122\mu\text{s}$), the LFI internal clock generator frequency. The clock drives synchronously the phase switches in the FEMs, the ADCs, and the on-board processor, which reconstructs the ordering of the acquired signals and synchronises it with the on-board time. Taking into account housekeeping and ancillary information, this corresponds to a data rate of ~ 5.7 Mbps, or a factor of 100 higher than the allocated data rate for the instrument, 53.5 Kbps. Averaging the samples from sky and reference load signals to within the Nyquist rate on the sky (3 bins per HPBW at each frequency) drastically reduces the data volume, leaving a compression requirement of a factor 2.4 (see Sect. 6). The adopted algorithm implemented in the SPU relies on three steps processing of nearly loss-less compression which requires 5-parameter tuning to be optimised (Maris et al. 2009).

The main functions of the data processing unit (DPU) include monitoring and control of the RAA, instrument initialisation, error management, on-board time synchronisation, management of instrument operating modes, control of the overall LFI data rate and data volume. Switch on/off of the FEMs and BEMs and voltage adjustments are addressed by the DPU with a configuration that allows a flexible commanding set-up. The DPU interface provides all commanding towards the DAE, while the SPU interface is in charge for retrieving the fixed format raw data from the

RCAs. Both the DPU and the SPU are based on a 18 MHz CPU. The link between the REBA and the DAE is implemented through IEEE 1355 interfaces and by means of data flag signals which ensure hardware and software synchronisation.

Finally, the data acquisition unit (DAU) is in charge of functions that are internal to the REBA and has no interfaces with the RAA. It converts the primary power received from the spacecraft to the secondary regulated voltages required by the REBA and it performs analog to digital conversion of REBA housekeeping data.

5. Thermal interfaces

5.1. LFI 20 K stage

The LFI front-end is cooled to 20 K by a closed-cycle hydrogen sorption cryo-cooler (Wade et al. 2000; Bhandari et al. 2004), which also provides 18 K pre-cooling to the HFI (Fig. 20). The cooler provides ~ 1 W of cooling power for the LFI FEU and sets an overall envelope to the heat load front end of the instrument. The cooler operates by thermally cycling a set of compressors filled with metal hydride $La_{1.0}Ni_{4.78}Sn_{0.22}$ that alternately absorb and desorb H_2 gas as their temperature is modulated, thus providing the working fluid in a Joule-Thomson (JT) refrigerator.

Heating of the sorbent beds is obtained by electrical resistance heaters, while its cooling is achieved by thermally connecting the compressor element to a radiator ~ 270 K in the warm spacecraft. The hydrogen flow-lines are intercepted by the three V-groove radiators and passively pre-cooled to ~ 50 K before reaching the 20 K JT expansion valve.

In the complete system, six identical compressors are used, each provided with a gas-gap heat switch to optimise thermal performance. An additional sorbent bed is used to damp pressure fluctuations of the low pressure gas. At any time, one compressor is hot and desorbing to provide the high pressure hydrogen gas, one compressor is cooling down, one is heating up, while the other three are cold and absorbing gas. This principle of operation ensures that no vibrations affect the detectors, a unique property of this kind of cooler which is very beneficial to Planck.

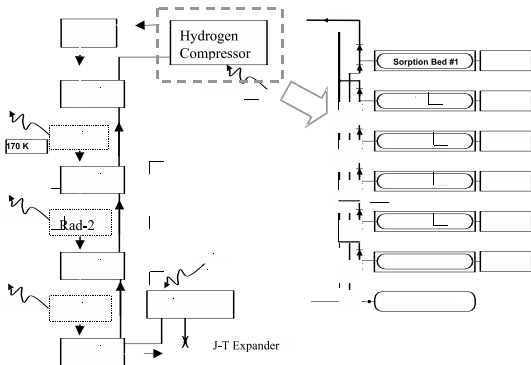


Fig. 20. (FIND BETTER FIGURE FOR SCS??) Schematic of the 20K sorption cooler, with the three pre-cooling V-groove radiators, four heat exchangers, the cold heads and the compressor. The arrows in front of each sorption bed represent check valves, allowing flow only in the arrow direction.

As a consequence of the cooler cycles the system exhibits two characteristic (controllable) time periods: τ_{bed} , synchronous with each sorbent bed cycle (nominally $\tau_{bed} = 667$ s), and $\tau_{system} = 6 \times \tau_{bed}$, for the whole system cycle.

Temperature fluctuations at the cold end are expected to modulate at these periods and may affect the LFI scientific performances both by direct coupling to the 20 K FPU and by fluctuations induced in the 4 K reference loads through the pre-cooling interface with HFI at 18 K. We analysed extensively this potentially serious source of systematic effects in the design phase by propagating its effects to the map level (Mennella et al. 2002b). We derived stringent requirements ($\delta T < 100$ mK peak-to-peak) on acceptable temperature fluctuations at the interfaces of the 20 K cooler with LFI (LVHX2), which would produce a highly deceptive effect on the data. Testing at instrument level (Tomasi et al. 2009a) and at system level have verified the design consistency.

5.2. Thermal loads

The limited cooling power of the sorption cooler imposes requirements on acceptable heat loads at 20 K. This includes power dissipated by the amplifiers and phase switches in the front-end, as well as parasitic loads from the waveguides, cryo-harness, and other passive elements. As discussed in **!!Section 4**, these were strong drivers in the architecture of the radiometer chains and in the design of the waveguides and cryo-harness (**!!Section 6**). Table 7 summarises the heat load budget at 20 K for the LFI elements. The 299 mW allocated to the front-end modules has been split in average dissipation of 31 mW per FEM at 30 and 44 GHz, and 24 mW per FEM at 70 GHz.

Table 7. 20 K heat load budget

Allocated power dissipation at 20 K	
FEMs	
(LNAs, phase switches)	299 mW
Waveguides	
(including support structure)	249 mW
Cryoharness	3 mW
Struts	23 mW
Radiant coupling	2 mW
Total	576 mW

As part of the system thermal design, upper limits to heat loads on each of the three V-grooves were allocated to the LFI. Table 8 shows the estimated loads from the LFI compared to the budget allocations, showing that compliance has been achieved with ample margins.

5.3. Temperature sensors

Temperature sensors are placed in strategic locations of the instrument flight model in order to monitor temperature values and fluctuations during both ground calibration (Morgante 2009; Tomasi et al. 2009a) and in-flight operation. A total of ?? sensors are used in LFI (Table 9). Fig. 21 shows the 12 sensors in the focal plane unit, 4 of which have higher sensitivity and lower dynamic range (up to 26.5 K) to adequately trace temperature fluctuations.

Table 8. Nominal heat loads from LFI and allocations at the three V-grooves

	Reference Temp.	Estimated heat load	Allocated heat load
VG3 (coldest shield)	51.4 K	463 mW	710 mW
VG2 (intermediate shield)	106.2 K	337 mW	560 mW
VG1 (warmest shield)	166.2 K	2939 mW	5370 mW

These are Lakeshore Silicon diode DT670 with typical sensitivity 15 mV/K at 20 K. One of the sensors (TS5R) has been placed on the flange of a 30 GHz feedhorn (RCA28) to directly monitor front-end stability. The interface to the sorption cooler cold end (LVHX2) is also monitored with sensors both on the LFI side and on the sorption cooler side. For analysis of in-flight data, additional temperature information will be used from sensors belonging to the HFI, the telescope and the spacecraft.

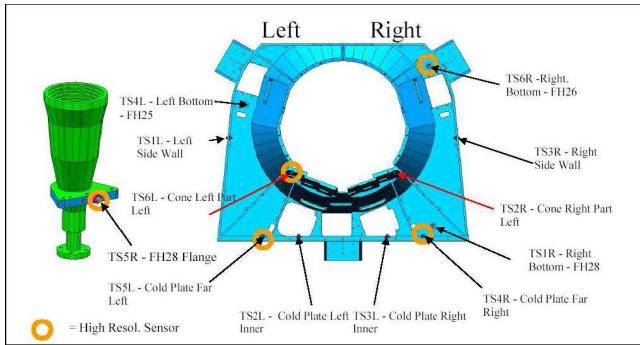
**Fig. 21.** Temperature sensors in the LFI front end unit. Circles indicate high sensitivity sensors.**Table 9.** Main LFI temperature sensors

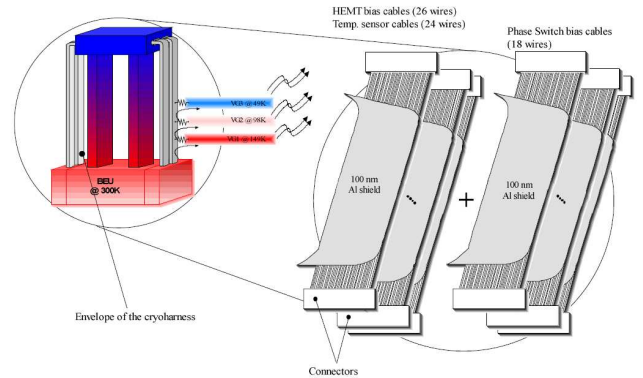
Table to be inserted here

6. Electrical and communication interfaces

6.1. Cryo-harness

A further challenging element in the LFI design is the electrical connection from the DAE power supply to the cryogenic front-end (cryoharness). Each FEM needs 22 bias lines for biasing the LNAs and phase switches. When including temperature sensor wires, a total of 290 lines have to be routed from the 300K electronics to the 20 K FPU along a path of ~ 2.2 m. The lines need to transport currents ranging from a few μA (for temperature sensors) up to 200 mA. The stability needed in the bias of the cryogenic LNAs call for high immunity to external noise and disturbances thus requiring efficient electrical shielding. On the

other hand, to minimise heat load at 20 K the heat transport needs to be kept at the few mW level. Furthermore, to ensure operability of LFI at room temperature (a tremendous advantage in the integration and test process), the harness was required to be compatible with operation at 300 K.

**Fig. 23.** Schematic of the cryoharness serving HEMT biasing, phase switch biasing and temperature sensors. Heat loads are minimised by interfaces with the V-grooves.

Frequency	Origin	Unit
1 Hz	HK acquisition frequency	DAE BEU
1 Hz	Synchronisation signal	DAE BEU, REBA
10 Hz	internal timer	SCS
1kHz	locking clocks	SCS
4096 Hz	Phase Switch frequency	FEM, DAE BEU
8192 Hz	Science data sampling frequency	DAE BEU
100 kHz	5V & 12V DC/DC	SCS
131072 Hz	DC/DC converters	DAE Power box
131072 Hz	On Board Clock signal	DAE BEU, REBA
131072 Hz	LOBT Clock	SCS
200 kHz	12V DC/DC	SCS
1 MHz	Command link from the BEU Box	DAE Power box
1 MHz	Internal transfer of digital data	DAE BEU, REBA
8 MHz	ADC clock	SCS
10/80 MHz	1355 serial data digital interface	DAE BEU, REBA
16 MHz	DSP processor clock	SCS
17.46 MHz	Clock frequency of the DSP	REBA
20 MHz	Sequencer internal clock	DAE BEU

Table 11. List of the LFI characteristic internal frequencies.

A dedicated trade-off study was carried out to identify proper materials and dimensions (**Leutenegger et al. 2003**). Table 10 shows the main characteristics of the identified solution, while Fig. 23 is a schematic of the cryoharness configuration and routing. The cryo-harness was

mounted as part of the RAA and integrated before delivery, so that it could be kept integrated.

6.2. Electromagnetic compatibility (EMC)

Great effort has been made to ensure highly stable electrical environment. The grounding scheme (Fig. 22) has been optimised to ensure maximum protection of the bias lines to the front-end cryogenic LNAs and phase switches. Table 11 lists all the internal frequencies of the LFI instrument and sorption cooler. Whenever relevant, these have been monitored in the test campaign as potential sources of RF disturbances, both within LFI and towards the HFI detectors.

6.3. Data rate

The choice of a far-earth orbit for Planck induces stringent requirements on the rate of data transmission to the ground. Both the sky and reference load samples will be transmitted to the ground, so that full data reduction can be performed at the LFI Data Processing Centre (DPC). After sample-averaging and data compression (by factor 2.4) performed in the REBA SPU (Sect. 4.4.3), the science data volume is 35.55 Kbps, increased to 37.15 Kbps due to packeting overheads. An additional 2.57 Kbps of uncompressed data comes from the so-called “calibration channel” (for diagnostics purposes, one LFI channel at the time will be transmitted to the ground without compression). When adding 2.41 Kbps of housekeeping, leads to a total budget of 42.13 Kbps for LFI, which is well within the allocated 53.5 Kbps (see Table 12). It is critical that the (average) 2.4 compression factor be achieved with an essentially lossless process, which requires careful optimisation of the parameters that control the on-board compression algorithm in the SPU Tomasi et al. (2009b). After telemetry transmission the data will be treated through LFI DPC “Level 1” (Frailis 2009) for real-time assessment, housekeeping monitoring, data de-compression. Then the time-order information (TOI) will be generated and processed by the successive analysis steps in the DPC pipeline (Zacchei et al 2009).

Table 12. LFI data rate summary

Frequency	30 GHz	44 GHz	70 GHz
Number of detectors	8	12	24
Angular resolution	33'	22'	14'
Beam crossing time (ms)	92	64	39
Sampling rate (Hz)	32.6	46.8	76.9
Science data rate (Kbps)	8.35	17.96	59.02
Science data rate	85.33 Kbps		
Science data rate after compression	35.55 Kbps		
Total LFI data rate	42.13 Kbps		

7. Optical interfaces

The optimisation of the optical interface between the combined LFI-HFI focal plane and the Planck telescope was coordinated throughout the various development phases of the project (Tauber et al 2009b). The final LFI optical design is discussed by Sandri et al. (2009) (and Maffei et al 2009 for the analogous process for HFI). Rejection of systematic effects arising from non-ideal optical coupling has been a major design driver for LFI (Mandolesi et al. 2000b; Villa et al. 2009c). Minimisation of beam ellipticity, particularly relevant for the off-axis LFI feeds, has been a key element in the optical design (Burigana et al. 1998; Sandri et al. 2009). An upper limit $< 1 \mu\text{K}$ to straylight contamination from various sources was set to provide a design criterion. Far sidelobe effects were simulated for the Sun, the Earth, the Moon and the Galactic plane (Burigana et al. 2001). The full beam pattern was calculated using a combination of physical optics (PO) and physical theory of diffraction (PTD) by considering radiation scattered by both reflectors.

Emission originating within the Planck spacecraft and coupling directly into the LFI beams (“internal straylight”) was also considered in the optical design as potential sources of systematic effect (ref?). An overall upper limit $1\mu\text{K}$ was set for internal straylight and a breakdown of contributions from various PPLM optical elements (baffle, reflectors structures, third V-groove) was carried out. Simulations have shown compliance with the allocated budget.

Knowledge of the optical transmission of the LFI channels is an essential element for the extraction of polarisation information (Leahy et al 2009) and for component separation. The band shapes of each RCA channel have been evaluated from measurements at single unit level combined with a dedicated software model, and verified with end-to-end testing as part of the RCA cryogenic test campaign (Zonca et al. 2009).

Alignment requirements on the FPU relative to the telescope were developed taking into account the thermo-elastic effects of the cooldown to 50 K of the LFI struts. The driving requirements were set by the HFI optical alignment which were more stringent due to the shorter wavelengths. For the LFI, the internal alignment requirements between FEU and BEU of $\pm 2 \text{ mm}$ required careful design of the waveguides supporting structures.

8. Systematic error budget

Limits on systematic effects impacting the effective angular resolution (beam ellipticity, alignment, pointing errors) were used as input to the design of the Planck telescope and focal plane, as well as pointing requirements at system level. From the goal limit $< 3 \mu\text{K}$ cumulative systematic error per pixel (Sect. 2.5) we defined a breakdown of contributions from various kinds of effects (Table 13) More detailed allocations were worked out for each contribution. This provided a useful guideline for the design, development and testing of the various LFI subsystems. For each type of systematic error we specify limits for three cases: a high frequency component, spin-synchronous fluctuations and periodic (non-spin-synchronous) fluctuations. High frequency contributions ($\gg 0.016 \text{ Hz}$) can be considered as random fluctuations and add in quadrature to the radiome-

ters white noise. As a goal, the overall noise increase due to random effect other than radiometer white noise should be less than 10%. Spin synchronous (0.016 Hz) components are not damped by scanning redundancy, and impose the most stringent limits to systematic effects. Periodic fluctuations on time scales other than the satellite spin are damped with an efficiency that depends on the characteristic time scale of the effect (see Mennella et al. (2002a) for quantitative analysis).

Table 13. Top level budget of LFI systematic errors. The allocated limits are residuals after consolidated software removal techniques are applied to the data

Source	Random % of $\delta T_{1-\text{sec}}$	Spin synch μK	Periodic μK
External Straylight	N/A	1	N/A
Internal Straylight	0.045	1	0.9
4K load	0.026	1	0.6
LFI thermal fluctuations	0.031	0.8	1.1
Front end 1/f	0.217	N/A	N/A
Back end 1/f	0.453	N/A	N/A
DC electronics	0.04	N/A	N/A
Quantisation	0.01	N/A	N/A
Total	0.507	1.9	1.5
Noise increase	0.121		

9. Conclusions

The Planck scientific objectives call for full-sky maps with sensitivity $\Delta T/T \approx 2 \times 10^{-6}$ per $\Delta\theta \approx 10'$ pixel. The combination of LFI and HFI cover the spectral range 30 to 850 GHz, which allow precise removal of non-cosmological emissions. The two instruments use widely different technologies and will be affected differently by different sources of systematic effects. This unique feature of Planck provides a powerful tool to identify and remove systematic effects. The Planck-LFI covers three frequency bands centred at 30, 44 and 70 GHz. The LFI is sensitive to polarisation in all channels, a characteristic of coherent detectors which does not call for any additional component or system compromise. The 70 GHz channel is near the minimum of the foreground emission, thus probing the cleanest cosmological window with an angular resolution of $13'$. The 30 and 44 GHz channels are sensitive to the cosmological signal but also are sensitive to synchrotron, free-free and anomalous dust diffuse radiation from the Galaxy. Thus they will serve as cosmological and foreground monitors in the Planck observations.

The LFI design required several challenging trade offs involving thermal, mechanical, electrical and optical aspects (Table 14). The cryogenic front-end receivers, required for high sensitivity, dominate the instrument performances and their interface with HFI is a major driver of the instrument configuration. The combination of the pseudo-correlation scheme and of the 4 KHz switching of the phase shifters in the FEM allow to obtain excellent stability while maintaining a highly modular design. Stringent requirements on noise temperature, 1/f noise, thermal and electrical stability, bandwidth, polarisation isolation, para-

Table 14. Some of the main requirements and design solutions in LFI

Requirement /constraint	Design solution
High sensitivity	Cryogenically cooled (~ 20 K) HEMT LNAs
Low residual 1/f, immunity from receiver systematics	Pseudo-correlation differential design Cryogenic reference load (~ 4 K) Offset removal by gain modulation factor in post-processing Fast switching (4 KHz) of sky and reference signal to suppress back-end 1/f noise
Single telescope	“Internal” reference signal
Modularity, cryo testing	Phase switch in front-end modules
Low power dissipation on 20 K stage	Two amplification stages (cold front-end and warm back-end) Low loss and thermal conductivity interconnecting waveguides
Waveguide mechanical routing	Phase switch and second hybrid in the front-end (avoids need of phase matched waveguides)

sitic heat loads were key elements in the design. A further key driver in the LFI design has been the control of systematic effects, which has also been a central part of the LFI calibration plan and test campaigns, both on-ground and in-flight. The functionality and performance of LFI was tested at various stages of development and integration (component level, unit level, RCA, instrument and satellite level). As discussed in Mennella et al. (2009) and Villa et al. (2009a), the performances measured in the instrument-level calibration campaign are in line with the design expectations.

Acknowledgements. Planck is a project of the European Space Agency with instruments funded by ESA member states, and with special contributions from Denmark and NASA (USA). The Planck-LFI project is developed by an International Consortium lead by Italy and involving Canada, Finland, Germany, Norway, Spain, Switzerland, UK, USA. The Italian contribution to Planck is supported by the Italian Space Agency (ASI). The work in this paper has been supported by in the framework of the ASI-E2 phase of the Planck contract. TP’s work was supported in part by the Academy of Finland grants 205800, 214598, 121703, and 121962. TP thank Waldemar von Frenckells stiftelse, Magnus Ehrnrooth Foundation, and Väisälä Foundation for financial support.

References

- Artal, E., Aja, B., L. de la Fuente, M., et al. 2009, A&A, this volume
- Battaglia, P., Bersanelli, M., Butler, R., et al. 2009, A&A, this volume
- Bhandari, P., Prina, M., Bowman, R. C., et al. 2004, Cryogenics, 44, 395
- Burigana, C., Maino, D., Górski, K. M., et al. 2001, A&A, 373, 345
- Burigana, C., Maino, D., Mandolesi, N., et al. 1998, A&As, 130, 551
- Cuttaia, F., D’Arcangelo, O., Stringhetti, L., et al. 2009, A&A, this volume
- D’Arcangelo, O., Figini, L., Simonetto, A., et al. 2009, A&A, this volume
- D’Arcangelo, O., Garavaglia, S., Simonetto, A., et al. 2003, Experimental Astronomy, 16, 165

- Davis, R., Wilkinson, A., Davies, R., et al. 2009, A&A, this volume
- Frailis, M. 2009, A&A, this volume
- Hoyland, R. 2003, in *ESA Workshop on Millimetre Wave Technology and Applications*, Vol. 211, Proceedings of 3rd ESA Workshop on Millimetre Wave Technology and Applications, 305–310
- Jarosik, N. 1996, *IEEE Trans. on Microwave Theory and Techniques*, 44, 193
- Maino, D., Burigana, C., Górski, K. M., Mandolesi, N., & Bersanelli, M. 2002, A&A, 387, 356
- Mandolesi, N., Aja, B., Artal, E., et al. 2009, A&A, this volume
- Mandolesi, N., Bersanelli, M., Burigana, C., et al. 2000a, A&A Suppl., 145, 323
- Mandolesi, N., Bersanelli, M., Burigana, C., & Villa, F. 2000b, *Astrophysical Letters Communications*, 37, 151
- Maris, M., Bersanelli, M., D’Arcangelo, O., et al. 2009, A&A, this volume
- Mennella, A. & Bersanelli, M. 2001, *Impact of Back-End temperature fluctuations on LFI PLANCK-LFI*, Tech. Rep. PL-LFI-PST-TN-029, IASF-MI-CNR
- Mennella, A., Bersanelli, M., Aja, B., et al. 2009, A&A, this volume
- Mennella, A., Bersanelli, M., Burigana, C., et al. 2002a, A&A, 384, 736
- Mennella, A., Seiffert, M., & Bersanelli, M. 2002b, *Temperature stability requirements of the LFI Sorption Cooler cold-end (LR2)*, Tech. rep., IASF-MI-CNR
- Morgante, G. 2009, A&A, this volume
- Penzias, A. A. & Wilson, R. W. 1965, *ApJ*, 142, 419
- Sandri, M., Bersanelli, M., Mennella, A., et al. 2009, A&A, this volume
- Seiffert, M., Mennella, A., Burigana, C., et al. 2002, A&A, 391, 1185
- Staggs, S. T., Jarosik, N. C., Wilkinson, D. T., & Wollack, E. J. 1996, *ApJ*, 458, 407
- Tomasi, M., Cappellini, B., Gregorio, A., et al. 2009a, A&A, this volume
- Tomasi, M., Mennella, A., Galeotta, S., et al. 2009b, A&A, this volume
- Valenziano, L., De Rosa, A., Cuttaia, F., et al. 2009, A&A
- Varis, J., Hughes, N., Laaninen, M., et al. 2009, A&A, this volume
- Villa, F., Bersanelli, M., Cappellini, B., et al. 2009a, A&A, this volume
- Villa, F., D’Arcangelo, O., Pagana, E., et al. 2009b, A&A, this volume
- Villa, F., D’Arcangelo, O., Pecora, M., et al. 2009c, A&A, this volume
- Villa, F., Sandri, M., Mandolesi, N., et al. 2002, *Experimental Astronomy*, 14, 1
- Wade, L., Bhandari, P., Bowman, J. R., et al. 2000, in *Advances in Cryogenic Engineering*, ed. et al. Kluwer Academic/Plenum New York Q-S. Shu, Vol. 45A, 499–506
- Zonca, A., Franceschet, C., Battaglia, P., Villa, F., & Mennella, A. 2009, A&A

Table 2. Sensitivity budget for LFI units at the three frequencies

		30 GHz	44 GHz	70 GHz
Feed + OMT insertion loss (dB)	$L_{\text{Feed}}L_{\text{OMT}}$	0.25	0.25	0.25
FEM noise temperature (K)	$T_{\text{noise}}^{\text{FE}}$	8.6	14.1	25.7
$T_{\text{Feed+OMT}} + T_{\text{FE}}$ (K)		10.4	16.2	28.5
Overall FEM gain (dB)	G_{FE}	>30	>30	>30
WG insertion loss (dB)	L_{WGs}	2	3	4
BEM noise temperature (K)	$T_{\text{noise}}^{\text{BE}}$	350	350	450
$T_{\text{WGs}} + T_{\text{BE}}$ (K)		0.3	0.4	0.7
T_{sys} (K)		10.7	16.6	29.2

Table 5. Main specifications of the front-end modules

	30 GHz	44 GHz	70 GHz
Band [GHz]	27-33	39.6-48.4	63-77
Noise temperature over band	8.6K	14.1K	25.7K
Gain (average over band)	30-33 dB	30-33 dB	30-33 dB
Gain ripple	< 5dB	< 5dB	< 5dB
Gain variation with physical temperature	0.05 dB/K	0.05 dB/K	0.05 dB/K
Gain variation with physical temperature	0.8 K/K	0.8 K/K	0.8 K/K
1/f knee frequency	< 20 mHz	< 20 mHz	< 20 mHz
X-polarisation	> 35 dB	> 35 dB	> 35 dB
Average power dissipation per FEM	31 mW	31 mW	24 mW

Table 10. Main characteristics and specifications of the LFI cryoharness

	Requirements					Design solution		
	N	$Max\ curr.$ <i>at 20 K</i>	$Max\ curr.$ <i>at 300 K</i>	$Electrical$ <i>resistance</i>	$Material$	$AWG\ diam$ <i>(mm)</i>	$Electrical$ <i>resistance</i>	$Power\ at$ <i>FPU</i>
HEMT GND	11	40 mA	200 mA	< 1 Ω	Copper	38 (0.1)	0.6 Ω	6.32 mW
HEMT Drain	44	10 mA	50 mA	< 5 Ω	Nickel	38 (0.1)	2.2 Ω	11.37 mW
HEMT Gate	88	100 μ A	100 μ A	< 200 Ω	Manganin	40 (0.08)	193.4 Ω	1.86 mW
Phase Switch GND	11	4 mA	4 mA	< 10 Ω	Titanium	32 (0.2)	5.2 Ω	1.55 mW
Phase Switch	88	1 mA	1 mA	< 50 Ω	Titanium	38 (0.1)	21.0 Ω	5.88 mW
Shield		N/A	N/A	N/A	Aluminium (+ Kapton)	100 nm	N/A	2.28 mW
Temp. Sensors	48	40 μ A	40 μ A	< 200 Ω	Manganin	40 (0.08)	139.3 Ω	0.93 mW
TOTAL	290							30.20 mW

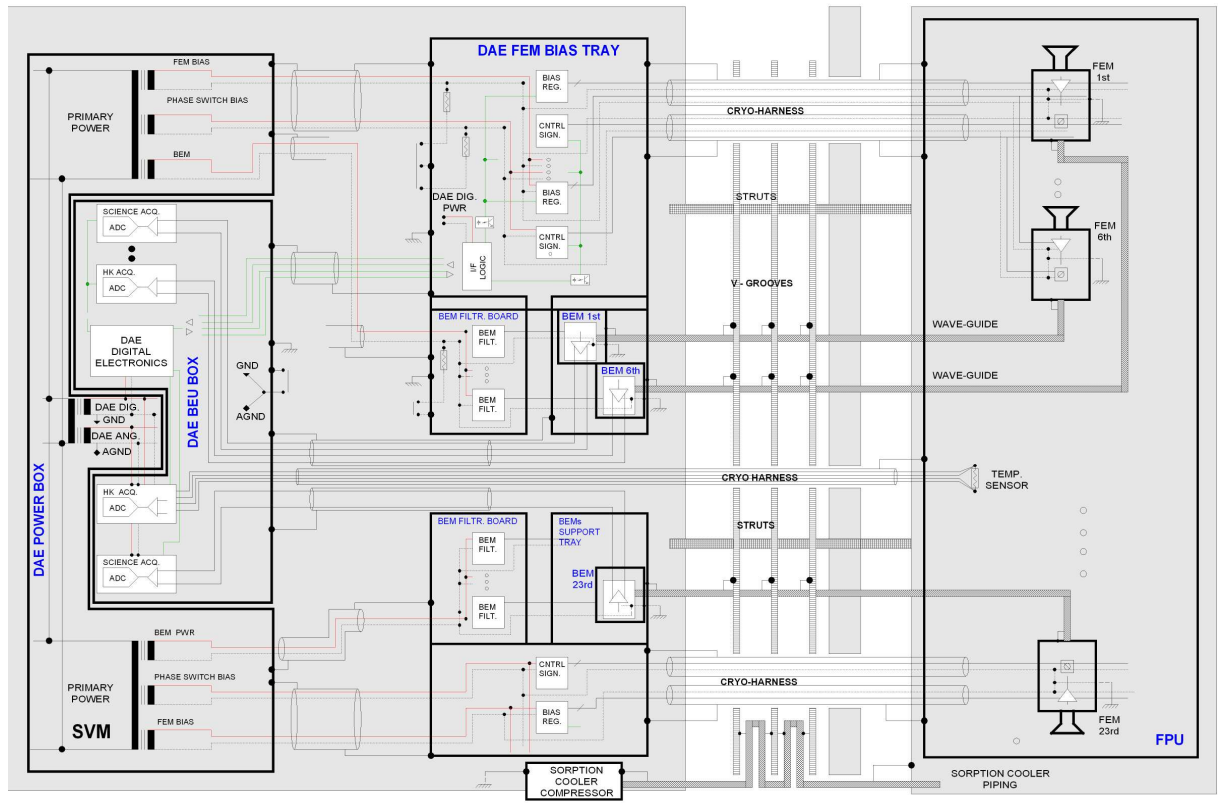


Fig. 22. Schematic of the grounding scheme of LFI